CHALMERS


**Publication 01/07**

# Large-Eddy Simulation of Turbulent Channel Flow Significantly Affected by Buoyancy

**Dalibor Čuturić**

*D*epartment of Thermo and Fluid Dynamics
CHALMERS UNIVERSITY OF TECHNOLOGY
Göteborg, Sweden, September 2001

# Abstract

This report forms a part of the project "**L**arge **E**ddy **S**imulation (**LES**) of Turbulent Flows Driven or Significantly Affected by Buoyancy".

In this work we validate first the LES code by means of the simulation of a fully developed turbulent horizontal channel flow with uniform heating at the both walls. In this flow the buoyant force in the streamwise direction is zero and the Reynolds number, $Re_\tau$, based on friction velocity and half channel width is $395$. The LES results are shown in good agreement with DNS data.

Then, to study mixed convection flow, simulation of the fully developed turbulent vertical channel flow with prescribed wall temperatures is done. In this flow the Reynolds number ($Re_\tau$) is $150$ and the buoyancy effect is significant.

The Smagorinski eddy-viscosity model was used to model the subgrid-scales of turbulent motion with a van Driest type damping function which account for viscosity effect near the walls.

All computations are performed using a finite volume code which is second-order accurate with central differencing in space and Crank-Nicolson scheme in time. The solution is processed using an implicit, two-step time-advancement method. The code is parallelized on the loop level using compiler directives (it works only on shared-memory computers). For all computation uses 4 processors on Chalmers' 64-processor CRAY 2000 Origin machine.

**Key Words:** Large Eddy Simulation (LES), Turbulent flow, Buoyancy, Heat transfer, Subgrid-scale (SGS) model, Channel flow.

## Acknowledgments

This report was carried out at the Department of Thermo and Fluid Dynamics at Chalmers.

First, I would like to thank to my supervisors Professor Lars Davidson and Assistant Professor Shia-Hui Peng for their support, help and well-informed advice.

I wish to thank all the personal at the Department of Thermo and Fluid Dynamics at Chalmers.

And finally, I want to thank my son, Deni, my wife, Elizabeta and my parents, for their love and support.

# Notation

## Symbols

| | |
|---|---|
| $\boldsymbol{x}, \boldsymbol{X}$ | Boldface letters are used for vectors, matrices and tensors. |
| $c_p$ | Specific heat at constant pressure. $[J/kgK]$ |
| $c_v$ | Specific heat at constant volume. $[J/kgK]$ |
| $Gr$ | Grashof number, $\frac{g\beta\triangle T(2\delta)^3}{\nu^2}$ |
| $g$ | Gravitational acceleration, $g = 9.81$. $[m/s^2]$ |
| $g_i$ | Gravitational vector, $g_i = (-g, 0, 0)$. |
| $Pr$ | Prandtl number, $\frac{\nu}{\alpha}$ |
| $Pr_t$ | Turbulent Prandtl number, $\frac{\nu_t}{\alpha_t}$ |
| $p$ | Pressure, $[N/m^2]$ |
| $e$ | Total energy per unit volume, $\rho c_v T + \frac{1}{2}(\rho u_i u_i)$ |
| $h$ | The fluid entalpy, $h = e + \frac{p}{\rho}$ |
| $q$ | Heat flux $[W/m^2]$ |
| $Re_b$ | Bulk Reynolds number, $\frac{2U_b\delta}{\nu}$ |
| $Re_\tau$ | Reynolds number based on friction velocity , $\frac{u_\tau\delta}{\nu}$ |
| $t$ | Time. $[s]$ |
| $T$ | Temperature. $[^oC]$ |
| $T_c$ | Temperature on the cooled wall. |
| $T_h$ | Temperature on the heated wall. |
| $T_{ref}$ | Reference temperature, $\frac{T_h+T_c}{2}$ |
| $T_\tau$ | Friction temperature on each wall, $\frac{q_w}{\rho c_p u_\tau}$ |
| $S_{ij}$ | Strain-rate tensor. |
| $BF$ | Body forces (Buoyancy, etc.) per unit volume $[N/m^3]$. |
| $\Phi$ | Dissipation function, $\tau_{ij}\frac{\partial u_i}{\partial x_j}$ |
| $u_i$ | Velocity. $[m/s]$ |
| $u_\tau$ | Friction velocity, $\sqrt{\frac{\tau_w}{\rho}}$ $[m/s]$. |
| $u_\tau^*$ | Friction velocity calculated from the wall shear stress averaged on the two walls. $[m/s]$ |
| $x_i$ | Space coordinates. $[m]$ |

## Greek

| | |
|---|---|
| $\delta$ | Channel half width. $[m]$ |
| $\alpha$ | Thermal diffusivity, $\frac{\kappa}{\rho c_p}$. $[W/m^2K]$ |
| $\alpha_t$ | Turbulent (SGS) thermal diffusivity, $\frac{\nu_t}{Pr_t}$. $[W/m^2K]$ |
| $\beta$ | Volumetric expansion coefficient. $\frac{1}{273.15+T_{ref}}, [^oK]$ |
| $\rho$ | Density of the fluid. $[kg/m^3]$ |
| $\mu$ | Dynamic viscosity. $[kg/ms]$ |
| $\kappa$ | Molecular conductivity. $[W/mK]$ |
| $\triangle T$ | Temperature difference, $T_h - T_c$. |
| $\epsilon$ | Dissipation rate. $[m^2/s^3]$ |
| $\nu$ | Kinematic viscosity. $[m^2/s]$ |
| $\nu_t$ | Turbulent (SGS) viscosity.$[m^2/s]$ |
| $\tau$ | Shear stress. $[Pa]$ |
| $\delta_{ij}$ | Kronecker delta. |

## Superscripts

| | |
|---|---|
| $(\,)^*$ | Normalized by $\delta$ and $u_\tau^*$. |
| $(\,)^+$ | Normalized by local $u_\tau$, $\nu$ and local $T_\tau$. |
| $(\,)'$ | Fluctuation component. |
| $\overline{(\,)}$ | Statistically averaged. |
| $(\,)^{dl}$ | Dimensionles variables. |
| $\langle\,\rangle$ | Averaged over the $x-z$ plane and time. |

## Subscripts

| | |
|---|---|
| $(\,)_{rms}$ | Root-Mean-Square fluctuation. |
| $(\,)_i$ | Index for tensor notation, $1, 2$ or $3$ $(x, y, z)$ |
| $(\,)_w$ | Wall value. |
| $(\,)_b$ | Bulk value. |
| $(\,)_t$ | Turbulent value. |
| $(\,)_{ref}$ | Reference value. |
| $(\,)_{per}$ | Periodic value. |
| $(\,)_{lin}$ | Linearly value. |

# Contents

# List of Figures

# List of Tables

# 1 Introduction

## 1.1 The Turbulence

Turbulence is a phenomenon that occurs commonly in nature, and turbulent modeling is one of the three key issues in Computation Fluid Dynamics (CFD). The other two keys are numerical method where very precise mathematical theories are developed and boundary conditions.

Turbulence is generally three dimensional and time dependent. For a complete description of turbulent flows we need an enormous amount of information. However in most practical applications, we only need to know the mean flow properties. Simple applications may require only the heat-transfer coefficient. More esoteric applications may need detailed knowledge such as energy spectra, turbulence fluctuations and flow structure.

Numerical or even analytical solution of turbulent flows may be accomplished using different levels of approximations yielding more or less detailed description of the state of the flow. One of the simplest methods is to use semi-empirical correlations. More sophisticated methods involving application of Reynolds averaging to the equations of motion, the well-known Reynolds-averaged Navier-Stokes equations (RANS) approach, which describes the evaluation of mean flow quantities. A Reynolds stress term, $\overline{u_i' u_j'}$, appears as an effect of turbulent fluctuations, and needs to be modeled to close the system of equations. The principal drawback of this approach is that the model represent the "mean" turbulence using averaged scales. While the small scales tend to depend only on viscosity, and may be somewhat universal, the large scales are affected very strongly by the boundary conditions. Thus, there is no universal RANS model to accurately different turbulent flows.

Direct numerical simulation (DNS) of turbulence is the most straightforward approach to the solution of turbulent flows. In DNS the governing equations are directly solved. If the mesh is fine enough to resolve even the smallest scales of motion and the scheme is designed to minimize the numerical dispersion and dissipations errors, then an accurate three-dimensional, time-dependent solution of the governing equations completely free of modeling assumptions can be obtained. The only error in this solution is that introduced by the numerical approximation. With the DNS method it is possible to compute and visualize any quantity of interest, including those that are difficult or even impossible to measure in experiments.

But there are some limitations of this method. If we resolve all scale of motions well, we need a number of grid points $N \sim L/\eta$, where $L$ is dimension of computational domain, and $\eta$ is the smallest scale of motion, the Kolmogorov length scale. This ratio is proportional to $Re^{3/4}$, which gives a number of grid points ($N$) in 3D required by DNS proportional to $N \sim Re^{9/4}$, and the time steps required to advance the computation is of the order of $Re^{3/4}$.

The total cost of a direct simulation is $Re^3$. Thus, to increase the Reynolds number by a factor of two, the computational effort must increase by at least a factor eight. This is a serious limitation for the use of DNS.

The Large-Eddy simulations (LES) technique is a method in between DNS and RANS. In a LES the contribution of the large, energy-carrying structures to momentum and energy transfer is computed directly, and only the effect of the smallest scale of turbulence is modeled.

## 1.2 The Buoyancy Force

The presence of a temperature difference in a pressure-driven flow field gives rise to density differences and thus a buoyancy force. The buoyancy force influences the turbulent transport heat and momentum in a mixed convection flow. The buoyancy-affected flow is referred to as aiding or opposing flow, depending upon whether the buoyancy force is acting to aid or to oppose the forced convection flow.

# 2 Turbulence Models

## 2.1 The Navier-Stokes Equations

The LES and the RANS are similar to the DNS in that they provide a three-dimensional, time dependent solution of the Navier-Stokes equations on a reasonably fine mesh.

The equations governing the conservation of mass, momentum and energy in a Newtonian fluid are[1]:

$$\frac{\partial \rho}{\partial t} + \frac{\partial}{\partial x_i}(\rho u_i) = 0 \tag{2.1}$$

$$\frac{\partial}{\partial t}(\rho u_i) + \frac{\partial}{\partial x_j}(\rho u_i u_j) = -\frac{\partial p}{\partial x_i} + \frac{\partial}{\partial x_j}\left[\mu\left(2S_{ji} - \frac{2}{3}\delta_{ij}S_{kk}\right)\right] + BF \tag{2.2}$$

$$\frac{\partial(\rho h)}{\partial t} + \frac{\partial}{\partial x_j}(\rho u_j h) = \frac{\partial}{\partial x_j}\left[\kappa\left(\frac{\partial T}{\partial x_j}\right)\right] + S_\phi \tag{2.3}$$

$$S_\phi = \Phi + \frac{\partial p}{\partial t} + \frac{\partial(u_j p)}{\partial x_j} \tag{2.4}$$

$$S_{ij} = \frac{1}{2}\left(\frac{\partial u_i}{\partial x_j} + \frac{\partial u_j}{\partial x_i}\right) \tag{2.5}$$

Assuming constant density and $\nu = \mu/\rho$ for incompressible flows we have:

$$\frac{\partial u_i}{\partial x_i} = 0 \tag{2.6}$$

$$\frac{\partial u_i}{\partial t} + \frac{\partial}{\partial x_j}(u_i u_j) = -\frac{1}{\rho}\frac{\partial p}{\partial x_i} + \nu\frac{\partial^2 u_i}{\partial x_j \partial x_j} + BF \tag{2.7}$$

$$\frac{\partial T}{\partial t} + \frac{\partial(u_j T)}{\partial x_j} = \alpha\frac{\partial^2 T}{\partial x_j \partial x_j} + S_\phi \tag{2.8}$$

[1] All equations are written in Cartesian tensor notation

where the term $\frac{\partial}{\partial x_j}\left(2\overline{S}_{ij}\right)$, using continuity, $\frac{\partial}{\partial x_j}\left(\frac{\partial \overline{u}_j}{\partial x_i}\right) = 0$, can be written as:

$$\frac{\partial}{\partial x_j}\left(\frac{\partial \overline{u}_i}{\partial x_j} + \frac{\partial \overline{u}_j}{\partial x_i}\right) = \frac{\partial^2 \overline{u}_i}{\partial x_j \partial x_j} \tag{2.9}$$

## 2.2 The Reynolds Averaging

The Reynolds averaging operation results in the Reynolds stresses. The Reynolds stresses are the unknowns in the governing equation and represent the reason for a discipline called turbulence modeling. The Reynolds decomposition splits each quantity ($u_i, T, p, etc.$) into its mean and fluctuating parts:

$$\Phi = \overline{\Phi} + \phi^{'} \tag{2.10}$$

Note that the mean part is written with an over-bar $\overline{\Phi}$.

Applying the Reynolds averaging, the mean part is time-averaged according to:

$$\overline{\Phi}(\mathbf{x}, t) = \frac{1}{\triangle T}\int_{t'}^{t'+\triangle T} \Phi(\mathbf{X}, t + t')dt' \tag{2.11}$$

## 2.3 The Large-Eddy Simulation

A Large-Eddy Simulation is a technique in which we decomposite the turbulent flow into two parts. The first one is large eddies which are resolved (computed) and the second one characterized by subgrid-scales (SGS) eddies which are modeled.

The large eddies are directly affected by the boundary conditions and they carry most of the turbulent energy. The small-scale turbulence is relatively weaker and it contributes only to a small part of the Reynolds stress and therefore is less critical.

LES involves modeling the small subgrid scale eddies and the smallest finite-volumes cells can be much larger than the Kolmogorov length [6] and time-steps can be much larger than in DNS. Hence, for a given

computation cost, it is possible to achieve much higher Reynolds numbers with LES than with DNS.

A major difficulty in Large-Eddy Simulation is that near a solid surface all eddies are small – to the extent that stress-bearing and dissipation ranges of eddy size overlap.

### 2.3.1 The Filtering Operation in LES

In LES the filtering operation is used, which filters out all scales smaller than the filter size.

The simplest type of filter is the volume-average filter implemented by Schumann [13]:

$$\overline{\Phi}(\mathbf{x},t) = \frac{1}{\triangle^3}\int_{x-\frac{1}{2}\triangle x}^{x+\frac{1}{2}\triangle x}\int_{y-\frac{1}{2}\triangle y}^{y+\frac{1}{2}\triangle y}\int_{z-\frac{1}{2}\triangle z}^{z+\frac{1}{2}\triangle z}\Phi(\mathbf{X},t)d\xi d\eta d\zeta \tag{2.12}$$

where $\triangle^3 = \triangle x \triangle y \triangle z$ corresponding grid increments of the finite-volume (or finite difference) equations.

Similar to RANS in a LES we decomposite $\Phi$ as:

$$\Phi = \overline{\Phi} + \phi \tag{2.13}$$

where filtered variables are function of space and time. The $\phi$ denotes a subgrid-scale component. Resolvable-scale component, or large-scale variable, denoted by over-bar ($\overline{\Phi}$), is defined as:

$$\overline{\Phi}(\mathbf{x}) = \int_D \Phi(\mathbf{x}^{'})G(\mathbf{x},\mathbf{x}^{'})d\mathbf{x}^{'} \tag{2.14}$$

where $D$ is the entire domain and $G$ is a low-pass filter function which determines the size of the small scales.

The most commonly-used filter functions inslude the sharp Fourier cutoff filter defined in wave space as [11]:

$$\hat{G}(k) = \begin{cases} 1 & \text{if } k \leq \pi/\Delta \\ 0 & \text{otherwise} \end{cases}, \tag{2.15}$$

the Gaussian filter:

$$G(x) = \sqrt{\frac{6}{\pi\Delta^2}}\ \exp\left(-\frac{6x^2}{\Delta^2}\right) \tag{2.16}$$

and top-hat filter:

$$G(x) = \begin{cases} 1/\Delta & \text{if } |x| \leq \Delta/2 \\ 0 & \text{otherwise} \end{cases} \tag{2.17}$$

In practice, the Gaussian filter is used in conjunction with a sharp Fourier cutoff filter in Fourier transforms and spectral methods. In this work, we use the top-hat filter in real space.

### 2.3.2 Filtered Navier-Stokes Equations

In adopting the filtering (in LES) operation one can use the following important properties:

$$\overline{\frac{\partial \Phi}{\partial x_i}} = \frac{\partial \overline{\Phi}}{\partial x_i}, \quad \overline{\overline{\Phi}} \neq \overline{\Phi}\ , \quad \overline{\phi} \neq 0, \quad \overline{\Phi\phi} \neq \overline{\Phi} \cdot \overline{\phi} \text{ and } \overline{\overline{\Phi}\phi} \neq 0 \tag{2.18}$$

The filtering operation (2.17) and (2.18)[2] applied on the governing equations (2.6-2.8) gives the filtered continuity equation and transport equation for momentum and thermal energy. These governing equations take the following form:

$$\frac{\partial \overline{u}_i}{\partial x_i} = 0 \tag{2.19}$$

$$\frac{\partial \overline{u}_i}{\partial t} + \frac{\partial}{\partial x_j}(\overline{u_i u_j}) = -\frac{1}{\rho}\frac{\partial \overline{p}}{\partial x_i} + \nu \frac{\partial^2 u_i}{\partial x_j \partial x_j} + \overline{BF} \tag{2.20}$$

$$\frac{\partial \overline{T}}{\partial t} + \frac{\partial (\overline{u_j T})}{\partial x_j} = \alpha \frac{\partial^2 \overline{T}}{\partial x_j \partial x_j} + \overline{S}_\phi \tag{2.21}$$

Equation 2.20 can be rewritten as:

$$\begin{aligned} &\frac{\partial \overline{u}_i}{\partial t} + \frac{\partial}{\partial x_j}(\overline{u_i u_j}) + \left[\frac{\partial}{\partial x_j}(\overline{u}_i \overline{u}_j) - \frac{\partial}{\partial x_j}(\overline{u_i u_j})\right] = \\ &-\frac{1}{\rho}\frac{\partial \overline{p}}{\partial x_i} + \nu \frac{\partial^2 u_i}{\partial x_j \partial x_j} + \left[\frac{\partial}{\partial x_j}(\overline{u}_i \overline{u}_j) - \frac{\partial}{\partial x_j}(\overline{u_i u_j})\right] + \overline{BF} \end{aligned} \tag{2.22}$$

[2]For uniform filter width, $\triangle$, the filters are mesh-preserving and commute with differentiation.

Equations (2.22) becomes:

$$\frac{\partial \overline{u}_i}{\partial t} + \frac{\partial}{\partial x_j}(\overline{u}_i \overline{u}_j) = -\frac{1}{\rho}\frac{\partial \overline{p}}{\partial x_i} + \nu \frac{\partial^2 \overline{u}_i}{\partial x_j \partial x_j} - \frac{\partial \tau_{ij}}{\partial x_j} + \overline{BF} \tag{2.23}$$

where

$$\tau_{ij} = \overline{u_i u_j} - \overline{u}_i \overline{u}_j \tag{2.24}$$

is the subgrid-scale (SGS) stress term, which must be modeled.

Equations (2.19), (2.21) and (2.22) can be non-dimensionized defining the dimensionless variables as:

$$\begin{gathered} x_i^{dl} = \frac{x_i}{\delta} \quad u_i^{dl} = \frac{u_i}{u_\tau^*} \quad p^{dl} = \frac{p}{\rho {u_\tau^*}^2} \\ t^{dl} = \frac{t u_\tau^*}{\delta} \quad T^{dl} = \frac{T - T_c}{\triangle T} \end{gathered} \tag{2.25}$$

where $u_\tau^*$ is the friction velocity.

Buoyancy is modeled using Boussinesq [2] approximation as[3]:

$$\overline{BF} = -g_i \beta (\overline{T} - T_{ref}) \delta_{1i} \tag{2.26}$$

The Grashofs number, $Gr$, is defined as:

$$Gr = \frac{\triangle T (2\delta)^3}{\nu^2} g\beta \tag{2.27}$$

Equations (2.26 – 2.27) with $Re_\tau^* = \frac{u_\tau^* \delta}{\nu}$ gives a buoyancy term in non-dimensional form:

$$\overline{BF} = \frac{Gr}{8 {Re_\tau^*}^2} (\overline{T}^{dl} - T_{ref}^{dl}) \delta_{1i} \tag{2.28}$$

[3]Note that $g_i$ is a vector $(-g, 0, 0)$ and $g_i \delta_{ij}$ gives buoyancy contrubution only in the 1 direction (or $x$).

Finally one has the governing equations in non-dimensional form (superscript $^{dl}$ will be dropped from the non-dimensional variables for convenience):

$$\frac{\partial \overline{u}_i}{\partial x_i} = 0 \tag{2.29}$$

$$\frac{\partial \overline{u}_i}{\partial t} + \frac{\partial}{\partial x_j}(\overline{u}_i \overline{u}_j) = -\frac{\partial \overline{p}}{\partial x_i} + \nu \frac{\partial^2 \overline{u}_i}{\partial x_j \partial x_j} - \frac{\partial \tau_{ij}}{\partial x_j} - \frac{Gr}{8\ Re_\tau^{*2}}(\overline{T}^{dl} - T_{ref}^{dl})\delta_{1i} \tag{2.30}$$

$$\frac{\partial \overline{T}}{\partial t} + \frac{\partial (\overline{u}_j \overline{T})}{\partial x_j} = \frac{1}{Pr Re_\tau^*} \frac{\partial \overline{T}}{\partial x_j \partial x_j} \tag{2.31}$$

## 2.4 Subgrid-Scale (SGS) Modeling

To model the scales of turbulent motion which are not resolved, we need a subgrid model. The main role of this model is to remove energy from the resolved scales (associated with the energy cascade). It is thus necessary to model the SGS stress so that the dissipative effect is well captured.

### 2.4.1 Eddy Viscosity Models

Most subgrid scale models in use are eddy-viscosity models, based on a gradient-diffusion hypothesis (similar to the Boussinesq hypothesis of RANS turbulence models [2]), which take the following form:

$$\tau_{ij} - \frac{1}{3}\delta_{ij}\tau_{kk} = -2\nu_T \overline{S}_{ij} \tag{2.32}$$

where $-\frac{1}{3}\delta_{ij}\tau_{kk}$ is the trace to make the equation valid upon contraction (i.e. setting the indices $i = j$) and $\delta_{ij}$ is the Kronecker delta defined as:

$$\delta_{ij} = \begin{cases} 1 & \text{if } i = j \\ 0 & \text{otherwise} \end{cases} \tag{2.33}$$

The subgrid-scale stresses, $\tau_{ij}$, are related to the large-scale strain-rate tensor

$$\overline{S}_{ij} = \frac{1}{2}\left(\frac{\partial \overline{u}_i}{\partial x_j} + \frac{\partial \overline{u}_j}{\partial x_i}\right) \tag{2.34}$$

The eddy viscosity, $\nu_T$, is in most cases obtained algebraically to avoid solving additional equations that could increase the cost of the calculations. It is hoped that a simple, algebraic model can describe the SGS physics reasonably, since the small scales tend to be more homogeneous and isotropic than the large ones. Modeling errors should not affect overall accuracy of the results as much as in the RANS turbulence modeling approach, since the subgrid-scale stresses only account for a small fraction of the total stresses and turbulent transport.

By dimensional analysis, the eddy viscosity has dimensions $m^2/s$, which can be expressed as the product of a length scale, $l$ $(m)$, and a velocity scale, $q_{SGS}$ $(m/s)$ where $C$ is a dimensionless constant of proportionality, i.e. [7]:

$$\nu_T = C \cdot l \cdot q_{SGS} \tag{2.35}$$

Most of the kinetic energy of turbulence is contained in the largest eddies and the turbulence length scale ($l$) is therefore characteristic of these eddies which interact with the mean flow. The most active unresolved scales are those which are closest to the cutoff.

A resonable length scale of SGS turbulence is the filter width, which is the size of the small structure in the flow, and is often proportional to the grid size. The velocity scale is usually taken to be the square-root of the trace of the SGS stress tensor, $q^2_{SGS} = \tau_{kk}$.

The local equilibrium assumption is made to simplify the problem further and obtain an algebraic model for the eddy viscosity so that we do not need to solve a transport equation to determine $q^2_{SGS}$. The equilibrium assumption is based on the consideration that the small scales of motion have shorter time scales than the large, energy-carrying eddies; thus it can be hypothesized that they adjust more rapidly than the largest scales to perturbations, and recover equilibrium nearly instantaneously. Under this assumption the transport equation for SGS kinetic energy is balanced by only two terms. The first one is the production of SGS energy, $\epsilon_{SGS} = -\tau_{ij}\overline{S}_{ij}$, which actually represent the

energy transfered from large scales. The second one is the viscous dissipation of SGS energy, $\epsilon_v$. This two terms are in balances, i.e. ( [11]):

$$\begin{aligned} \epsilon_v &= \epsilon_{SGS} \\ &\text{or :} \\ \epsilon_v &= -\tau_{ij}\overline{S}_{ij} \end{aligned} \tag{2.36}$$

### 2.4.2 Smagorinsky Model

The Smagorinsky model [14] is the eddy-viscosity model, and from historical point of view is the progenitor of all subgrid-scale stress models. The model is based on the equilibrium hypothesis (2.36). The viscous dissipation is modeled as $\epsilon_v \sim q_{SGS}^3/l$ with (2.36) using (2.32) and (2.35) gives:

$$q_{SGS} \sim l|\overline{S}| \tag{2.37}$$

where $|\overline{S}| = \sqrt{2\overline{S}_{ij}\overline{S}_{ij}}$ is the magnitude of the large-scale strain-rate tensor. Letting $l \sim \overline{\triangle}$ and taking the filter-width as the local grid size, one has:

$$\overline{\triangle} = (\overline{\triangle}_{x,i}\overline{\triangle}_{y,j}\overline{\triangle}_{z,k})^{1/3} = (V_{IJK})^{1/3} \tag{2.38}$$

where indices $i, j$ and $k$ denote cell-index in the three coordinate directions, and $V_{IJK}$ is the volume of the computational cell $i, j$ and $k$.

Now eddy viscosity can be written as:

$$\nu_T = (C_s\overline{\triangle})^2|\overline{S}| \tag{2.39}$$

where $C_s$ is Smagorinsky constant. The model is absolutely dissipative:

$$\epsilon_{SGS} = (C_s\overline{\triangle})^2|\overline{S}|^3 \geq 0 \tag{2.40}$$

The disadvantage of the Smagorinsky model is that the constant $C_s$ is problem dependent. Usually, this constant varies in the range of $0.065 \leq C_s \leq 0.25$. In the present work we use a value of $C_s = 0.1$.

### 2.4.3 Damping Functions

To avoid some problems in the wall region the Smagorinsky model needs special treatment. When one uses a subgrid scale model, the resolved strain does not vanish on the wall, while the SGS stress does. Therefore, the subgrid viscosity, $\nu_T$, must be forced to vanish at the walls. Often a damping function is applied to the turbulent viscosity to account for viscous effects near walls. This function dampens the time scale $l$ near the walls.

A van Driest type damping function is usually used:

$$f = 1 - e^{(-\frac{y^+}{A^+})} \tag{2.41}$$

where $A^+$ is a constant for which the value of 25 is used and $y^+$ is the distance from the nearest wall, given by:

$$y^+ = \frac{yu_\tau}{\nu} \tag{2.42}$$

Taking the near-wall damping into account, equation (2.39) can be rewritten as:

$$\nu_T = (C_s f\overline{\triangle})^2|\overline{S}| \tag{2.43}$$

# 3 Test Cases

The general objective of the work is to explore and model turbulent flows driven or significantly affected by buoyancy using large eddy simulation techniques. Two cases were selected for simulation in this work. In both cases we investigate channel flow with almost the same geometry, as shown in Figures 3.1 and 3.2. A mesh with $66 \times 66 \times 66$ nodes is used for both cases.

## 3.1 The Horizontal Channel Flow

In this case we have a fully developed turbulent channel flow with uniform heat fluxes at both walls. The Reynolds number, $Re_\tau$, based on the friction velocity and the channel half with is $395$, and the molecular Prandtl number is $0.71$. Channel length is $2\pi$, height is $2\delta$, $\delta = 1$ and width is $\pi/2$, .

In this case the temperature field is decoupled from the velocity field and the buoyancy term ($\overline{BF}$) in the momentum equation (2.20) is neglected.

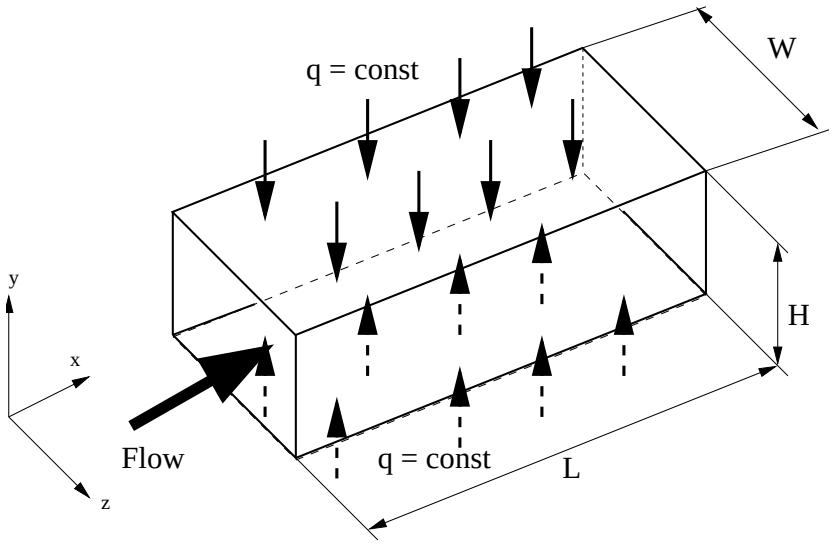


**Figure 3.1.** Computational domain for the horizontal channel flow

## 3.2 The Vertical Channel Flow

This flow is also a fully developed turbulent channel flow, but here we prescribe the wall temperatures. The Reynolds number, $Re_\tau^*$, based on the friction velocity calculated from the wall shear stress averaged on the two walls, $u_\tau^*$, and the channel half width, is $150$. The molecular

Prandtl number is $0.71$. Channel length is $5\pi$, height is $2\delta$, width is $2\pi$, $\delta$ is $1$ and the Grashofs number, $Gr$, is $9.6 \cdot 10^5$.

In this case the temperature field is coupled to the velocity field via the buoyancy term ($\overline{BF}$) in the momentum equation (2.20), see equation (2.30).

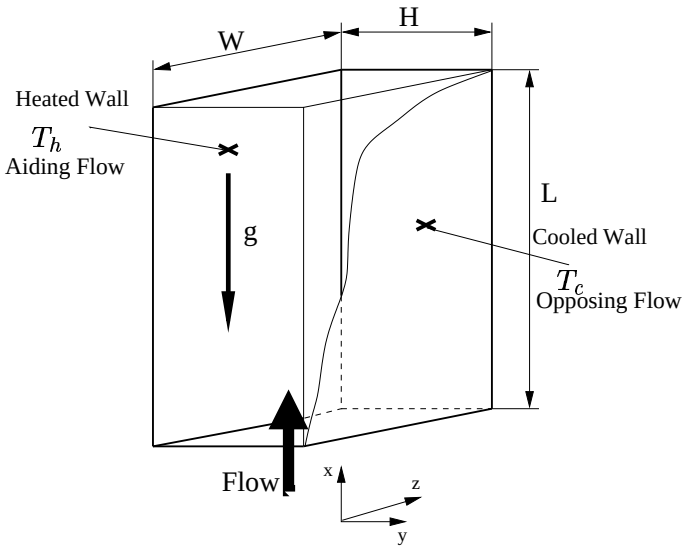


**Figure 3.2.** Computational domain for the vertical channel flow

# 4 Numerical Procedure

The code is based on the finite-volume method for solving the incompressible Navier-Stokes equations employing a non-staggered, collocated grid arrangement. Several numerical schemes for discretizing the convective term are incorporated into to code. In the present work we use the second-order central differencing scheme [10]. For time integration we use the second-order Crank-Nicolson scheme. The momentum and energy equations are solved with the point-wise symmetric Gauss-Seidel relaxation method whereas a multigrid V-cycle is used for the acceleration of convergence when solving the pressure equation. For more details, see [15] and [3].

Parallelized computations were carried out for this flow on a $64$-processor $CRAYORIGIN$ $2000$, the Silicon Graphics machine. The $LES$ code was paralleled by Zacharov [17]. Four processors are used in present work.

The filter box is used to distinguish the small scales from the turbulent motions. The width of the grid filter, $\triangle$, is the same as the mesh size.

## 4.1 The Finite Volume Method

The conservation law for the transport of scalar quantities in a unsteady flow has the general form [16]:

$$\frac{\partial}{\partial t}(\rho\phi) + div(\rho \mathbf{u}\phi) = div(\Gamma grad\phi) + S_\phi \tag{4.1}$$

By using Gauss' divergence theorem:

$$\int_{CV} div\mathbf{a}dV = \int_A \mathbf{n}\cdot\mathbf{a}dA \tag{4.2}$$

where $\mathbf{n}$ is the vector normal to surface element $dA$.

By changing the order of integration in the time derivative term, integrating of equation (4.1) over a control volume ($CV$) and a time step $\triangle t$, we obtain:

$$\begin{aligned}\int_{CV}\left[\int_t^{t+\triangle t}\frac{\partial}{\partial t}(\rho\phi)dt\right]dV+\int_t^{t+\triangle t}\left[\int_A \mathbf{n}\cdot(\rho\mathbf{u}\phi)dA\right]dt=\\ \int_t^{t+\triangle t}\left[\int_A \mathbf{n}\cdot(\Gamma grad\phi)dA\right]dt+\int_t^{t+\triangle t}\left[\int_{CV}S_\phi dV\right]dt\end{aligned} \tag{4.3}$$

To demonstrate the integration we use one-dimensional equation. This gives (see figure 4.1)

**Figure 4.1.** Location of nodes and control volume faces.

$$\begin{aligned}\int_w^e\left[\int_t^{t+\triangle t}\rho\frac{\partial\phi}{\partial t}dt\right]dV+\int_t^{t+\triangle t}\left[(\rho uA\phi)_e-(\rho uA\phi)_w\right]dt=\\ \int_t^{t+\triangle t}\left[\left(\Gamma A\frac{\partial\phi}{\partial x}\right)_e-\left(\Gamma A\frac{\partial\phi}{\partial x}\right)_w\right]dt+\int_t^{t+\triangle t}\overline{S}\triangle V dt\end{aligned} \tag{4.4}$$

where:

$$\int_{CV}\left(\int_t^{t+\triangle t}\rho\frac{\partial\phi}{\partial t}dt\right)dV=\rho(\Phi_P-\Phi_P^0)\triangle V \tag{4.5}$$

The source term $S$ may be approximated by means of a linear form:

$$\overline{S}\triangle V=S_u\ +\ S_P\phi_P \tag{4.6}$$

where $S_P\leq 0$ to increase the numerical stability. The diffusive flux term are evaluated as:

$$\begin{aligned}\left(\Gamma A\frac{d\phi}{dx}\right)_e&=\Gamma_e A_e\left(\frac{\phi_E-\phi_P}{\delta x_{PE}}\right)\\ \left(\Gamma A\frac{d\phi}{dx}\right)_w&=\Gamma_w A_w\left(\frac{\phi_P-\phi_W}{\delta x_{WP}}\right)\end{aligned} \tag{4.7}$$

Here the upper-case letter ($N \rightarrow north, E \rightarrow east, etc.$) index indicates node point and the lower-case letter ($n, e, s, etc.$) indicates face point, see figure 4.1.

Face values of diffusion coefficients $\Gamma$ are calculated as follows:

$$\Gamma_w = (1 - f_W) \cdot \Gamma_W + f_W \cdot \Gamma_P \tag{4.8}$$

where the interpolation factor $f_W$ is given by:

$$f_W = \frac{\delta x_{Ww}}{\delta x_{Ww} + \delta x_{wP}} \tag{4.9}$$

## 4.2 Numerical Method

With equations (4.2 – 4.9) the filtered Navier-Stokes equation (2.30) is integrated over a time step $\triangle t$ and a control volume ($CV$) so that [16]:

$$\begin{aligned} &\int_{CV} \left( \int_t^{t+\triangle t} \frac{\partial \overline{u}_i}{\partial t} dt \right) dV + \int_t^{t+\triangle t} \left( \int_{CV} \frac{\partial}{\partial x_j} (\overline{u}_i \overline{u}_j) dt \right) dV = \\ &- \int_t^{t+\triangle t} \left( \int_{CV} \frac{1}{\rho} \frac{\partial \overline{p}}{\partial x_i} dt \right) dV + \int_t^{t+\triangle t} \left( \int_{CV} \nu \frac{\partial^2 \overline{u}_i}{\partial x_j \partial x_j} dt \right) dV \\ &- \int_t^{t+\triangle t} \left( \int_{CV} \frac{\partial \tau_{ij}}{\partial x_j} dt \right) dV + \int_t^{t+\triangle t} \left( \int_{CV} BF dt \right) dV \end{aligned} \tag{4.10}$$

Integration of each term $\Psi_P$ with respect to time:

$$I_T = \int_t^{t+\triangle t} \Psi_P dt = [\alpha \Psi_P + (1 - \alpha) \Psi_P^0] \triangle t \tag{4.11}$$

where $\Psi_P^0$ refers to the value at time $t$, and $\Psi_P$ at time $t + \triangle t$ and where the weighting parameter $\alpha$ is $0.5$ (Crank-Nicolson).

Finally eq. (4.10) may be discretized as:

$$\begin{aligned} &\frac{\overline{u}_i^{n+1} - \overline{u}_i^n}{\triangle t} = \\ &\qquad \alpha \left[ -\frac{\partial}{\partial x_j} (\overline{u}_i^{n+1} \overline{u}_j^{n+1}) + \nu \frac{\partial^2 \overline{u}_i^{n+1}}{\partial x_j \partial x_j} - \frac{\partial \tau_{ij}^{n+1}}{\partial x_j} - \frac{1}{\rho} \frac{\partial \overline{p}^{n+1}}{\partial x_i} \right] \\ &(1 - \alpha) \left[ -\frac{\partial}{\partial x_j} (\overline{u}_i^n \overline{u}_j^n) + \nu \frac{\partial^2 \overline{u}_i^n}{\partial x_j \partial x_j} - \frac{\partial \tau_{ij}^n}{\partial x_j} - \frac{1}{\rho} \frac{\partial \overline{p}^n}{\partial x_i} \right] \end{aligned} \tag{4.12}$$

which gives:

$$\overline{u}_i^{n+1} = \overline{u}_i^n + \triangle t L_u \left(D_{u,c}^n, D_{u,c}^{n+1}\right) - \alpha \frac{\triangle t}{\rho} \frac{\partial \overline{p}^{n+1}}{\partial x_i} - (1-\alpha)\frac{\triangle t}{\rho}\frac{\partial \overline{p}^n}{\partial x_i} \quad (4.13)$$

where $L_u \left(D_{u,c}^n, D_{u,c}^{n+1}\right)$ represents the right-hand side in equation (4.12) except the pressure gradient term or:

$$\begin{aligned} L_u \left(D_{u,c}^n, D_{u,c}^{n+1}\right) = \alpha \left[-\frac{\partial}{\partial x_j}(\overline{u}_i^{n+1}\overline{u}_j^{n+1}) + \nu \frac{\partial^2 \overline{u}_i^{n+1}}{\partial x_j \partial x_j} - \frac{\partial \tau_{ij}^{n+1}}{\partial x_j}\right] \\ (1-\alpha)\left[-\frac{\partial}{\partial x_j}(\overline{u}_i^{n}\overline{u}_j^{n}) + \nu \frac{\partial^2 \overline{u}_i^{n}}{\partial x_j \partial x_j} - \frac{\partial \tau_{ij}^{n}}{\partial x_j}\right] \end{aligned} \quad (4.14)$$

$D_{u,c}$ denotes the central differencing approximation applied to these terms, and $\alpha = 1/2$ for the second-order Crank-Nicolson scheme. In a similar way, the filtered energy equation (2.31) is represented in its discrete form by:

$$\overline{T}_i^{n+1} = \overline{T}_i^n + \triangle t L_T \left(D_{T,c}^n, D_{T,c}^{n+1}\right) \quad (4.15)$$

The standard form of the control volume formulation of eq. (4.13) is:

$$\begin{aligned} a_P(\overline{u}_i)_P^{n+1} &= \alpha \sum a_{nb}(\overline{u}_i)_{nb}^{n+1} + b \\ b &= (1-\alpha)\sum a_{nb}(\overline{u}_i)_{nb}^n + \left[a_P^0 - (1-\alpha)\sum a_{nb}\right](\overline{u}_i)_P^n + S \\ a_P &= a_P^0 + \alpha \sum a_{nb} \\ a_P^0 &= \frac{\triangle V}{\triangle t} \end{aligned} \quad (4.16)$$

The source term $S$ includes the pressure terms, the buoyancy term (if appropriate) and one part of the subgrid stress given by $\frac{\partial}{\partial x_j}\left(\nu_T \frac{\partial \overline{u}_j}{\partial x_i}\right)$.

First, equation (4.13) is solved with the symmetric Gauss-Seidel method. To reinforce the velocity-pressure coupling, an approach similar to the Rhie-Chow interpolation [12] in the RANS computation is employed. An intermediate velocity field, $\overline{u}_I^*$, is computed by subtracting the implicit part of the pressure gradient from equation (4.13) giving:

$$\overline{u}_i^* = \overline{u}_i^{n+1} + \alpha \frac{\triangle t}{\rho} \frac{\partial \overline{p}^{n+1}}{\partial x_i} \tag{4.17}$$

Note that the intermediate velocity does not satisfy the continuity equation. To satisfy continuity a divergence is made for equation (4.17), where the velocity field is taken at the volume faces, $\overline{u}_{i,f}^{n+1}$, i.e., $\frac{\partial \overline{u}_{i,f}^{n+1}}{\partial x_i}$. This divergence leads to a Poisson equation for the pressure:

$$\frac{\partial^2 \overline{p}^{n+1}}{\partial x_i \partial x_i} = \frac{\rho}{\alpha \triangle t} \frac{\partial \overline{u}_{i,f}^*}{\partial x_i} \tag{4.18}$$

In equation (4.18), the velocity divergence is calculated using the intermediate velocity at the control volume faces obtained through linear interpolation from neighboring intermediate nodal velocities. This equation is solved with a multigrid method [4]. The resulting pressure field, together with the intermediate velocities, is then employed to obtain the velocity field which satisfies the continuity:

$$\overline{u}_{i,f}^{n+1} = \overline{u}_{i,f}^* - \alpha \frac{\triangle t}{\rho} \left( \frac{\partial \overline{p}^{n+1}}{\partial x_i} \right)_f \tag{4.19}$$

The resulting face velocity $\overline{u}_{i,f}^{n+1}$, is then used to compute the mass fluxes at cell faces. Then we can solve the energy equation (4.15). The SGS eddy viscosity and diffusivity are subsequently computed.

## 4.3 The Numerical Algorithm

The solution procedure can be summarized as follows:

1. Solve $\overline{u}_i$ from eq. (4.13).
2. To obtain the intermediate velocity fields $\overline{u}_i^*$, solve eq. (4.17).
3. Solve the Poisson equation (4.18).
4. Compute the face velocities $\overline{u}_{i,f}^*$ using eq. (4.19).
5. Repeat step 1 to 4 until convergence is reached
6. Use $\overline{u}_{i,f}^*$ to compute the mass fluxes at cell faces.
7. Solve the energy equation (4.15).
8. Compute turbulent viscosity $\nu_T$ and diffusivity.
9. Go to next time step ($t + \triangle t$).

## 4.4 Periodic Flow Condition

The cases examined here have a geometrical and flow pattern which identically repeats itself after a certain distance in the stream-wise ($x$) and in the spanwise ($z$) direction, i.e. the flow is periodic. These geometrical modules have identical inlet and outlet flow except for the pressure and the temperature field (in a case with constant heat flux). The reason why the pressure and the temperature do not repeat themselves in each module is that they continuously decay/increase along the stream-wise direction.

### 4.4.1 Pressure

To make the pressure periodic we do decomposition into a periodic term and a linearly varying term in the stream-wise direction, i.e.:

$$\overline{p}(x,z,t) = \overline{p}_{per}(x,z,t) + \frac{d\overline{p}_{lin}}{dx}x \tag{4.20}$$

where $\frac{d\overline{p}_{lin}}{dx} = -1$. Then, the $\frac{\partial \overline{p}}{\partial x}$ term in the momentum equation (2.30) can be written as:

$$-\frac{\partial \overline{p}}{\partial x_i} = -\frac{\partial(\overline{p}_{per} + \frac{d\overline{p}_{lin}}{dx}x\delta_{i1})}{\partial x_i} = -\frac{\partial \overline{p}_{per}}{\partial x_i} + \delta_{i1} \tag{4.21}$$

Note that the non-dimensional term, $\frac{d\overline{p}_{lin}}{dx} = 1$ because it balances the wall shear stresses $(\tau_{wl} + \tau_{wr})$.

### 4.4.2 Temperature

To make the temperature periodic (in the case with constant heat flux) we need to do some modifications in the governing equation (2.31). In a periodic flow regime, the temperature, $T$, can be decomposed, like pressure above, into a periodic term and a linearly varying term in the stream-wise direction, i.e.:

$$\overline{T}(x,z,t) = \overline{T}_{per}(x,z,t) + \frac{d\overline{T}_{lin}}{dx}x \tag{4.22}$$

where the periodic term, $\overline{T}(x,z,t)$, identically repeats it self in each module, and the linear temperature increase[4] is given by the heat flux and mass flow:

[4]The linear temperature term can be decreasing if it is a cooling case.

$$\frac{d\overline{T}_{lin}}{dx} = \frac{2q_w W}{\dot{m} c_p} \tag{4.23}$$

where $q_w$ is (constant) wall heat flux on one side and $W$ is channel width.

The $\rho\frac{\partial(\overline{u}_i\overline{T})}{\partial x_i}$ term in equation 2.31 with periodic condition can be written as:

$$\rho\overline{u}_i\frac{\partial\overline{T}}{\partial x_i} = \rho\overline{u}_i\frac{\partial\overline{T}_{per}}{\partial x_i} + \rho\overline{u}_i\frac{2q_w W}{\dot{m} c_p}\delta_{1i} \tag{4.24}$$

## 4.5 The Boundary Conditions

### 4.5.1 Cyclic (Homogeneous) Boundary

The inlet and outlet have periodic boundaries, as noted above, with the identity given as:

$$\begin{aligned} \Phi(ni) &= \Phi(2) \\ \Phi(1) &= \Phi(ni-1) \end{aligned} \tag{4.25}$$

where $\Phi$ will be the velocity components, $\overline{u}_i$, pressure, $\overline{p}_{per}$ and temperature, $\overline{T}_{per}$. From here on, subscript $_{per}$ will be dropped from the periodics variables for simplicity.

### 4.5.2 The Wall

At the walls no-slip condition were set and the Neuman condition is used for the pressure.

To reduce the turbulent viscosity, $\nu_T$, near the wall we use a damping function which was described in detail in Subsection 2.4.3.

## 4.6 The Time Advancement

The physical constraint requires $\triangle t$ to be less than the time scale of the resolved scale of motion, $\tau \approx \triangle x/U_c$ (where $U_c$ is convective velocity).

We use an implicit scheme in the present work. For values of time step see Table 5.1.

## 4.7 The Initial Conditions

For flows that are statistically steady, the initial condition are unimportant and the final steady state is not sensitive to the initial conditions. The vertical channel case requires a longer time than the horizontal one for the flow to develop, probably due to the buoyancy term which imposes a strong coupling between the temperature and the vertical velocity component.

To speed up the calculation, the initial conditions for the horizontal channel case were adopted from the isothermal simulation (fully developed channel flow). The temperature field for horizontal channel was started from scratch ($T = 0$, see fig. A.4) and for the vertical channel it was generated linearly through (see fig. A.11):

$$T = -(j-1) \cdot \frac{\triangle T}{nj-1} + T_H \tag{4.26}$$

where $j$ is index for node point, $1 \leq j \leq nj$, and $nj$ denotes number of nodes. Statistics are accumulated in time and homogeneous direction ($x$ and $z$) when steady state is reached, see fig. A.1 - A.14 in **Appendix A**.

# 5 Results

Two different cases are simulated in the present study.

The first case has prescribed constant wall heat flux on both walls, top and bottom (horizontal channel flow) with friction Reynolds number $395$. The second one (vertical channel flow), where the wall temperatures are constant but different, has the cold wall to the right ($y = -1$) and the hot wall to the left ($y = 1$). In this case the friction Reynolds number is $150$ and the Grashof number is $9.6 \cdot 10^5$.

The results are compared with the DNS results. Note that, in the vertical channel case, all quantities with superscript $^+$ are normalized by the friction velocity, $u_\tau$, (or/and the friction temperature $T_\tau$ and the temperature difference $\triangle T$) calculated on each wall.

The time per iteration and number of iterations for each time step are given in a table 5.1. One to two iterations per time step are required to reach convergence.

| $Case$ | $t_{iter}$ $[sec]$ | $N_{iter}$ | time step, $\triangle t$ | mesh DNS | mesh LES |
|---|---|---|---|---|---|
| hcf | $\approx 7.71$ | $\approx 2$ | $1.685\ E-03$ | $1264 \times 395 \times 632$ | $66 \times 66 \times 66$ |
| vcf | $\approx 11.2$ | $\approx 2$ | $5.732\ E-03$ | $128 \times 96 \times 128$ | $66 \times 66 \times 66$ |

**Table 5.1.** Horizontal channel = $hcf$, Vertical channel = $vcf$, time per iteration, $t_{iter}$ on 1 CPU, number of iterations, $N_{iter}$, per time step, time step, $\triangle t$ and mesh size.

## 5.1 Horizontal Channel Flow

### 5.1.1 Velocity Field and Shear Stress

The mean velocity field is shown and compared with DNS data [1] in figure 5.1, normalized by the maximal (channel-center) velocity and in figure 5.2, normalized with $u_\tau$, to examine the obtained velocity field. The $rms$ velocity fluctuation are shown and compared with DNS data in figure 5.3.

The velocity field shows a small disagreement with the DNS data in logarithmic region ($10^1 - 10^2$) in wall coordinates (figure 5.2) and in global coordinates ($0.05 - 0.4$), figure 5.1 , but agreement is good in general.

In figure 5.2 we can clearly see two regions:

- The inner region $0 < y^+ < 30$
- The log-law layer region $30 < y^+ < 300$

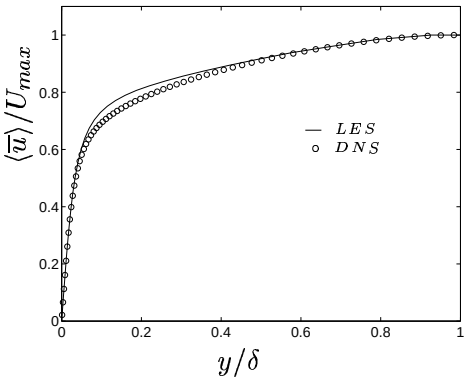


**Figure 5.1.** Mean velocity profile in comparison with DNS data [1], $Re_\tau = 395$.

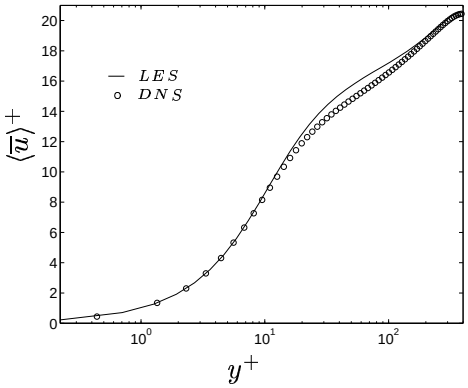


**Figure 5.2.** Normalized mean velocity profile in comparison with DNS data [1], $Re_\tau = 395$.

In the $rms$ of velocity components (figure 5.3), the LES data have a slightly over-predicted ($u^+_{rms}$) and under-predicted ($v^+_{rms}$ and $w^+_{rms}$) peak value respectively in comparison with DNS data but show good agreement in the region outer. The stream-wise velocity fluctuation, $u^+_{rms}$, in the near-wall region is much higher than the other two, and in the region outer their differences is much smaller. It means that the turbulent production mainly creates the stream-wise component, $u^+_{rms}$, which means that the turbulence is anisotropic in the near-wall region and in the region outer, where values are almost the same, the turbulence structures becomes more isotropic.

Distribution of the resolved Reynolds shear stress is shown in figure 5.4, where the LES gives slightly under-predicted values in the near-wall region and slightly over-predicted values in the outer region.

The largest velocity gradient is in the near-wall region where also the largest values of the $rms$ velocity fluctuations, $u^+_{i\,rms}$, and the Reynolds shear stress are found, $\langle uv\rangle^+$, (see figure 5.3 and 5.3), which means that the turbulence production is high in the near-wall region.

### 5.1.2 Mean Temperature and Temperature Variance

The mean temperature in wall coordinates is given in figure 5.5 in comparison with DNS data [1] and we can see a very good agreements in almost all regions. The $rms$ of the temperature variance is shown in figure 5.6 and there is a large peak in the near-wall region. Values of

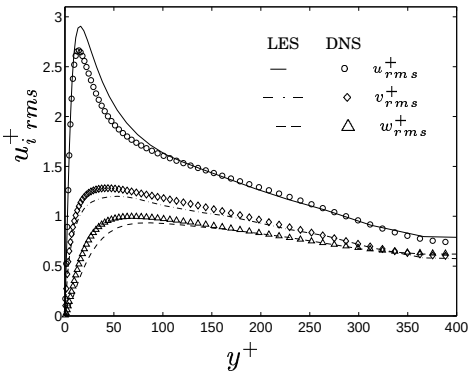


**Figure 5.3.** $u_{rms}$ velocity profile in comparison with DNS data [1], $Re_\tau = 395$.

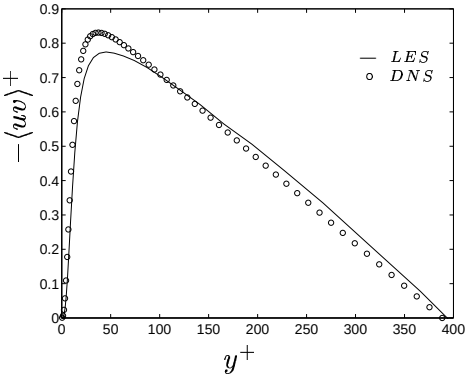


**Figure 5.4.** Resolved Reynolds shear stress in comparison with DNS data [1], $Re_\tau = 395$.

the $T_{rms}$ decrease in the outer region and becomes much smaller than in the near-wall region.

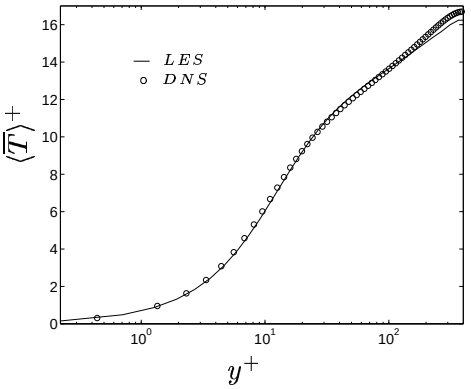


**Figure 5.5.** Mean temperature profile in comparison with DNS data [1], $Re_\tau = 395$.

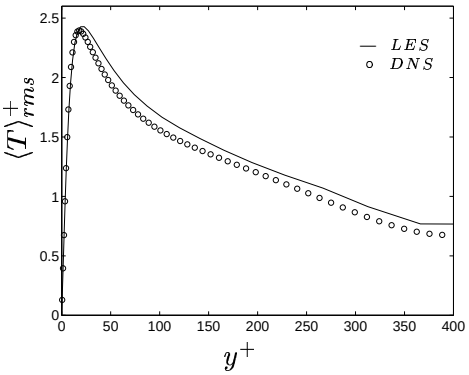


**Figure 5.6.** $Rms$ of the temperature profile in comparison with DNS data [1], $Re_\tau = 395$.

### 5.1.3 Turbulent Heat Flux

The stream-wise turbulent heat flux component is shown in figure 5.7 and the wall-normal component in figure 5.8.

The stream-wise heat flux has a peak closer to the wall than the heat flux in the wall-normal direction. This can be explained by the velocity fluctuations, where the wall-normal velocity fluctuation dampens strongly by the wall and have maximum value farther away than the velocity fluctuation in the stream-wise direction. The peak in the stream-wise direction is much steeper. Note that in region, $y^+ > 110$, the heat flux decreases with a very small gradient.

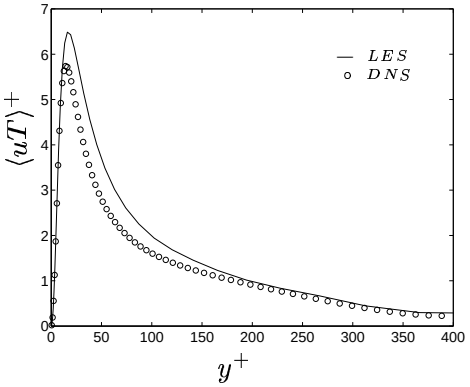


**Figure 5.7.** Turbulent heat flux vector in the stream-wise direction in comparison with DNS data [1], $Re_\tau = 395$.

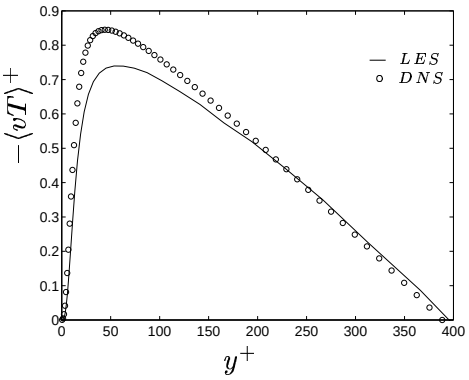


**Figure 5.8.** Turbulent heat flux vector in the wall-normal direction in comparison with DNS data [1], $Re_\tau = 395$.

## 5.2 Vertical Channel Flow

Before showing and analyzing the results in this case we would like to point out some problems which explain the following discussion and differences between the LES and the DNS data.

For comparison of our results with the existing DNS data ([5]) we choose to compute the fully developed channel flow with $Re_\tau^* = 150$, where $Re_\tau^*$ is calculated as: $Re_\tau^* = u_\tau^* \delta / \nu$. We choose $u_\tau^* = 1$ which gives $\nu = 1/Re_\tau^*$ (with $\delta = 1$).

The friction velocity, $u_\tau^*$, and the wall shear stress, $\tau_w^*$, are calculated by:

$$u_\tau^* = \sqrt{\frac{\tau_w^*}{\rho}}, \qquad \tau_w^* = \frac{1}{2}\left(\mu \frac{\partial U}{\partial y}\Big|_{y=-1} + \mu \frac{\partial U}{\partial y}\Big|_{y=1}\right) \tag{5.1}$$

Then, the force balances gives[5] $-\frac{\partial p}{\partial x} = \tau_w^* = \rho {u_\tau^*}^2 \delta = 1$.

The present results show that the value of the friction velocity is actually below one ($= 0.89$). The reason is that the net buoyancy force is not zero (see Section 5.2.4). So in our case the Reynolds bulk number ($Re_b = 4970$) is actually higher than in the DNS data ($4494$). This means that we calculate a case with larger bulk velocity, and smaller

[5]Note that the friction velocity is averaged on the **two** walls.

$Re_\tau^*$ ($\approx 133$). Thus our buoyancy term in the momentum equation (2.30) is smaller because in the buoyancy term which includes $1/Re_\tau^{*2}$ we have used $Re_\tau^* = 150$ and this is one reason why the present results are different than DNS data.

It is interesting to note that the calculated buoyancy term have negative values of the net buoyancy (negative direction in figure 5.27) which is probably related to the larger bulk velocity.

Possible correction of this problem are shown in Section 7.

In this work the focus was not on the discussion about the difference in values between the LES and the DNS, but rather on the behavior of the buoyancy and its effect on the flow.

A low-frequently oscillation in the bulk velocity profile was observed[6] which causes problem with choosing when the flow is in fully developed state (see figure A.13) and when the averages over space and time should take place. The averages process was starting a couple of times but every time in the averages process the bulk velocity drifted away from the "steady-state" value.

To reduce effect by the low-frequent oscillation in the bulk velocity the averages value was taken over a long time (over $23000$ time steps)[7]. That should gives a better mean values[8].

### 5.2.1 Velocity Field and Shear Stress

The mean velocity profile which is affected by buoyancy is shown in global coordinates (figure 5.9) and in local (wall) coordinates (figure 5.10).

The predicted $u_\tau$ at the hot and the cold wall are $u_{\tau h} = 0.9994$ and $u_{\tau c} = 0.7607$ respective and $u_\tau^* = 0.888$, calculated from the wall shear stress averaged on the two walls. Data from the present LES calculation are over-predicted as compared with the DNS data. The velocity profile in figure 5.9 is asymmetric because the temperature difference between the walls produces a positive buoyancy contribution on one side (hot-left) and negative buoyancy contribution on the other side (cold-

[6] This is probably related to the computational domain, which is not large enough to contain more than two flow modes in the assumed homogeneous directions.

[7] Corresponding to $t^{dl} > 130$ in dimensionless time or $t > 148$ $[sec]$.

[8] Here is noted that only mean velocity profile and all velocity quantities is sensitive to change in bulk velocity. All temperature quantities are much less sensitive and gives almost the same profile, see figures B.1 – B.11 in Appendix B.

right).

Figure 5.10 shows the velocity profile in the wall coordinates for opposite (negative buoyancy) and aiding (positive buoyancy) flow. Here we can see clearly the difference between aiding and opposing sides where opposing side has smaller values than the aiding side. It is also noted that a logarithmic region in aiding flow does not exist any longer, which is consistent with DNS data [5].

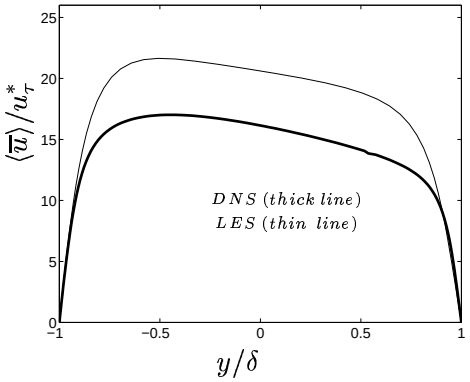


**Figure 5.9.** Mean velocity profile in global coordinates in comparison with DNS data [5], $Re_\tau = 133$.

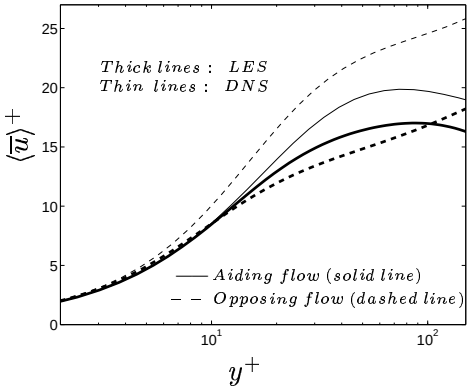


**Figure 5.10.** Mean velocity profile in wall coordinates in comparison with DNS data [5], $Re_\tau = 133$.

The $rms$ velocity fluctuations near the walls are shown in local (wall) coordinates, figure 5.11 - 5.13 and in global coordinates, figure 5.15 - 5.17. The $u_{rms}$ velocity profile has a peak near the walls, larger for opposing flow. The values of $v_{rms}$ and $w_{rms}$ are much smaller than $u_{rms}$. In comparison with isothermal (without buoyancy) flow, figure 5.3, we can see the similar behavior with more anisotropic turbulence in the near-wall region and the flow is more isotropic in the outer region. It is interesting to note that the LES gives much larger values of the fluctuation in the stream-wise direction (factor of 2) in the opposing flow and under-predicts values for the other velocity fluctuations (in comparison with the DNS). But always, the opposing flow fluctuations have larger values than the aiding flows (this does not depend on normalization, see figure 5.15 - 5.17).

The resolved Reynolds shear stress is shown in local (wall) coordinates, figure 5.14 in the near-wall region and in global coordinates, figure 5.18. It can be seen that the Reynolds shear stress, if we compare the aiding and the opposing side, at the opposing side have larger values (more than a factor of 2). This asymmetric behavior of the Reynolds shear stress can be clearly seen in figure 5.18 where zero value of $\langle uv\rangle/(u_\tau^*)^2$

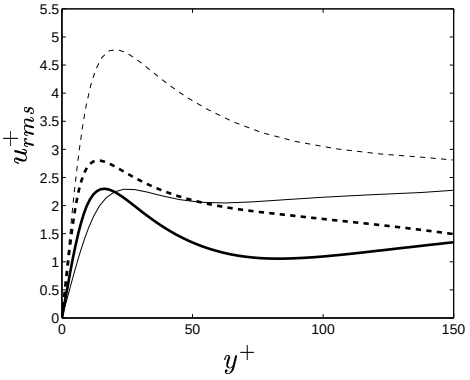


**Figure 5.11.** $u_{rms}$ velocity profile in comparison with DNS data [5], $Re_\tau = 133$. For legend, see figure 5.10

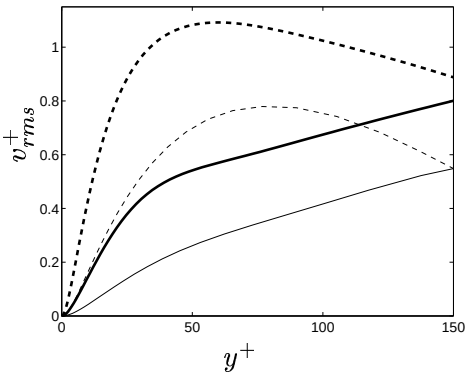


**Figure 5.12.** $v_{rms}$ velocity profile in comparison with DNS data [5], $Re_\tau = 133$. For legend, see figure 5.10

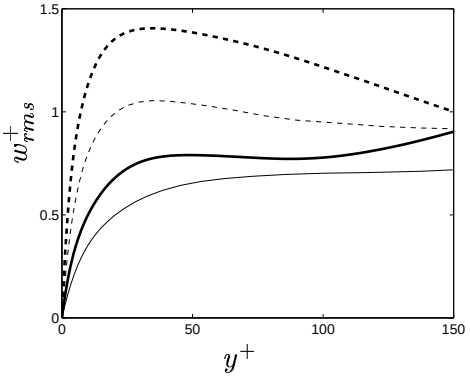


**Figure 5.13.** $w_{rms}$ velocity profile in comparison with DNS data [5], $Re_\tau = 133$. For legend, see figure 5.10

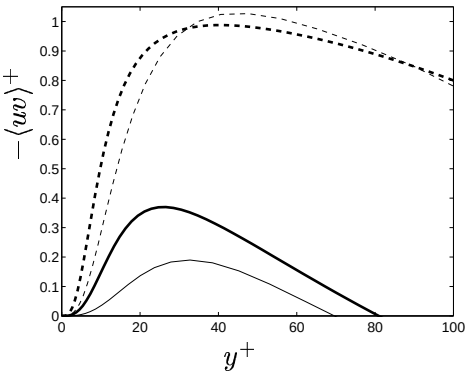


**Figure 5.14.** Resolved Reynolds shear stress in comparison with DNS data [5], $Re_\tau = 133$. For legend, see figure 5.10

is shifted to the left, which is discussed in section 5.2.4.

### 5.2.2 Temperature and Temperature Variance

The mean temperature profile is shown in global coordinates, figure 5.19 and in wall coordinates, figure 5.20. Agreement between the LES and the DNS data is much better than for the velocity components. It seems that the temperature distribution over the cross section is less sensitive to the bulk velocity. The temperature increase is the same on both sides in the near-wall region, see figure 5.20, and it is noted that the mean temperature $\langle T \rangle^+$ on the aiding flow side increases twice as much in comparison with the opposing side in region $y^+ > 10$.

The $rms$ fluctuation of the temperature is shown in local coordi-

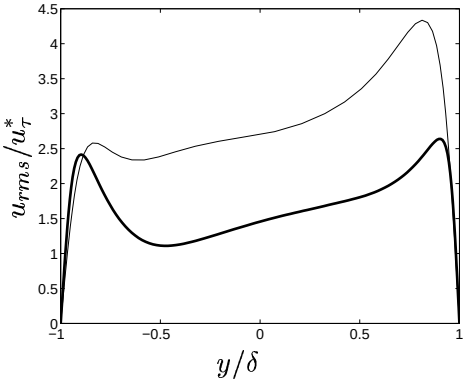


**Figure 5.15.** $u_{rms}$ velocity profile in global coordinates in comparison with DNS data [5], $Re_\tau = 133$. For legend, see figure 5.9

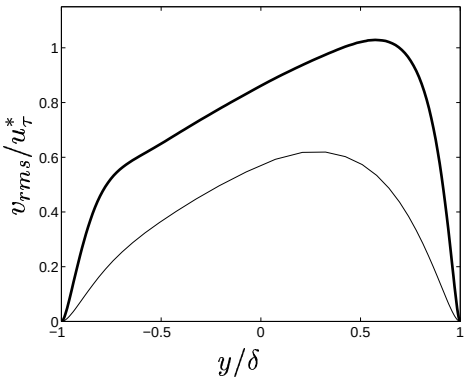


**Figure 5.16.** $v_{rms}$ velocity profile in global coordinates in comparison with DNS data [5], $Re_\tau = 133$. For legend, see figure 5.9

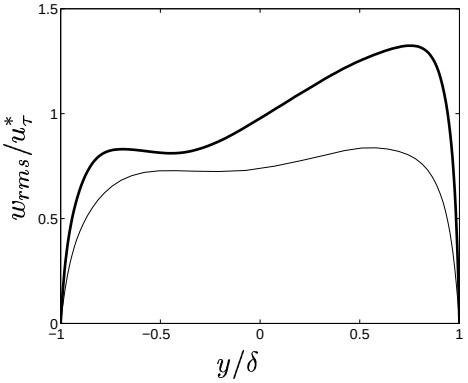


**Figure 5.17.** $w_{rms}$ velocity profile in global coordinates in comparison with DNS data [5], $Re_\tau = 133$. For legend, see figure 5.9

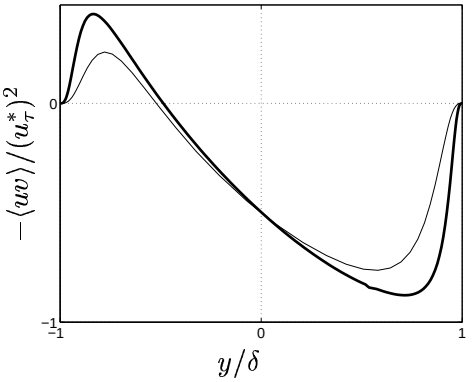


**Figure 5.18.** Resolved Reynolds shear stress in global coordinates in comparison with DNS data [5], $Re_\tau = 133$. For legend, see figure 5.9

nates, figure 5.21 and in global coordinates, figure 5.22. The temperature fluctuations increase in the near-wall region for the opposite and the aiding flow. Even in the outer region the aiding flow temperature fluctuation increases while the opposing decreases. In global coordinates, see figure 5.22, can be seen that the LES give more obvious peak values on the aiding side than the opposing side in comparison with DNS.

### 5.2.3 Turbulent Heat Flux

The turbulent heat flux in the local and the global coordinates are shown in the stream-wise direction, figure 5.23 and 5.25 respective and in the wall-normal direction, figure 5.24 and 5.26 respective. In the

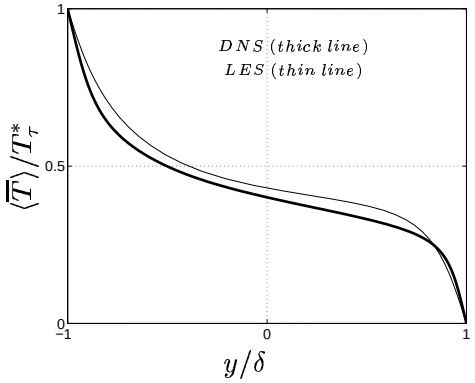


**Figure 5.19.** Mean temperature profile in comparison with DNS data [5], $Re_\tau = 133$.

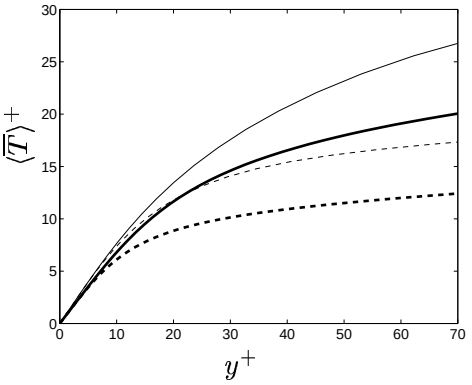


**Figure 5.20.** Mean temperature profile in wall coordinates, $Re_\tau = 133$. For legend, see figure 5.10

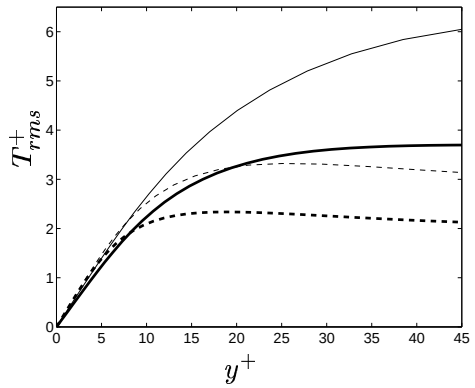


**Figure 5.21.** $Rms$ temperature profile in comparison with DNS data [5], $Re_\tau = 133$. For legend, see figure 5.10

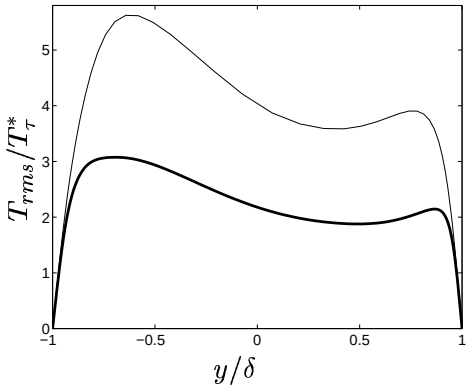


**Figure 5.22.** $Rms$ temperature profile in global coordinates in comparison with DNS data [5], $Re_\tau = 133$. For legend, see figure 5.9

stream-wise direction the flow has the same behavior with steep increasing in the near-wall region and then decreasing. It was also observed that the LES gives a good agreement in the near-wall region but in the region out-of-wall the LES gives larger values than the DNS. In the wall-normal direction the heat flux increase in the near-wall region and then becomes asymptotic (both for the opposite and the aiding side).

### 5.2.4 Balances of Transport Equations

By integrating the momentum equation (in the stream-wise direction) (2.30) with (4.20) from the hot to the cold wall ($0 \leq y \leq 2 \cdot \delta$), we obtain the equation for the stress balance in the stream-wise direction:

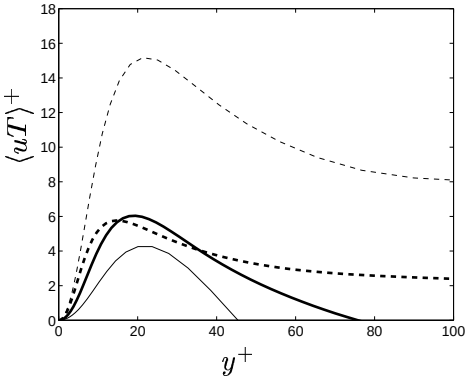


**Figure 5.23.** Turbulent heat flux vector in a stream-wise direction in comparison with DNS data [5], $Re_\tau = 133$. For legend, see figure 5.10

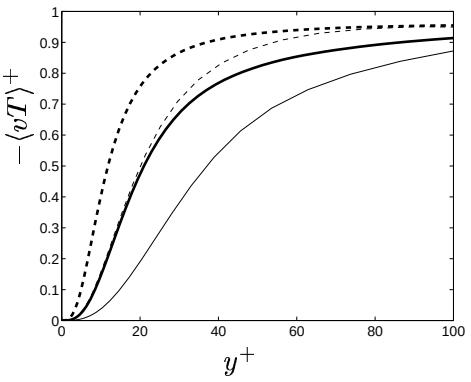


**Figure 5.24.** Turbulent heat flux vector in a wall-normal direction in comparison with DNS data [5], $Re_\tau = 133$. For legend, see figure 5.10

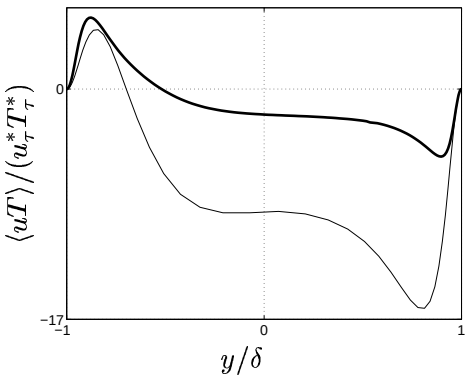


**Figure 5.25.** Turbulent heat flux vector in global coordinates in a stream-wise direction in comparison with DNS data [5], $Re_\tau = 133$. For legend, see figure 5.9

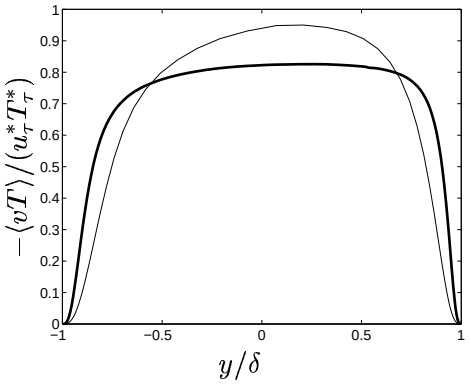


**Figure 5.26.** Turbulent heat flux vector in global coordinates in a wall-normal direction in comparison with DNS data [5], $Re_\tau = 133$. For legend, see figure 5.9

$$-\langle uv \rangle\Big|_y + \left\langle \nu \frac{\partial u}{\partial y} \right\rangle\Big|_y + \left\langle \nu_t \frac{\partial u}{\partial y} \right\rangle\Big|_y + \frac{Gr}{8 \cdot Re_\tau^{*2}} \int_0^y (T - T_{ref}) dy = \frac{\partial u}{\partial y}\Big|_{y=0} - y \tag{5.2}$$

where the terms on the left-hand side are the Reynolds shear stress, the viscous stress, the SGS stress and the buoyant force, respectively. The terms on the right-hand side are the wall shear stress and the prescribed driving force.

The force balance, see figure 5.27, in the $x-$ direction:

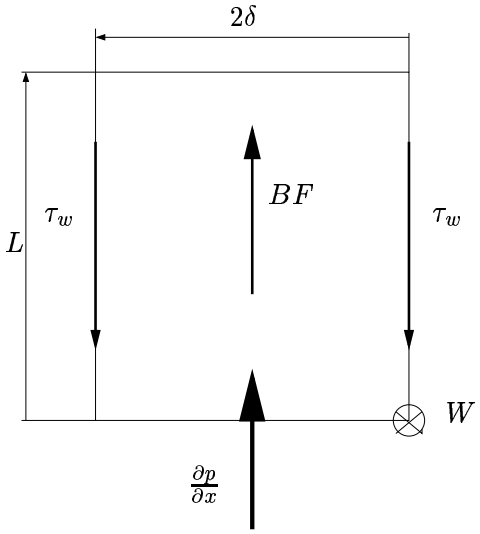


**Figure 5.27.** Force balance

$$\frac{\partial p}{\partial x} \cdot V_{x,y,z} - 2 \cdot \tau_w \cdot A_{x,z} + BF \cdot V_{x,y,z} = 0 \tag{5.3}$$

with $V_{x,y,z} = 2\delta \cdot L \cdot W$, $A_{x,y} = L \cdot W$, $\frac{\partial p}{\partial x} = 1$ and $\tau_w = \rho u_\tau^{*2}$ gives $BF = u_\tau^{*2} - 1$. Since $u_\tau^* < 1$, the net buoyancy force has a negative value, which can be seen in figure 5.29.

For isothermal flow (i.e. with no buoyancy) the integrated momentum equation (5.2) gives that the pressure gradient balances the sum of the Reynolds shear stress, SGS stress and the viscous stress and they are all symmetrical with different sign for the opposing and the aiding side, see figure 5.28.

The asymmetric behavior of the Reynolds shear stress in figure 5.14 can be explained by the influence of the buoyancy force on the mean flow.

The buoyancy force is not zero and it has a positive sign over almost the whole region. This leads to an increase of the magnitude of the Reynolds shear stress on the opposing side and a decrease on the aiding side, see figure 5.29 .

The budget equation of the resolved turbulent kinetic energy, $\langle k \rangle = \frac{1}{2}\langle u_i u_i \rangle$, is given as:

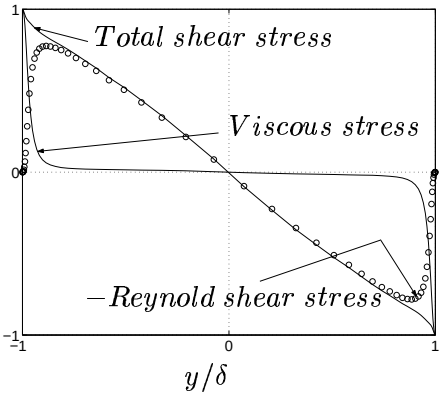


**Figure 5.28.** Stress balance in a wall-normal direction (horizontal channel), $Re_\tau = 395$.

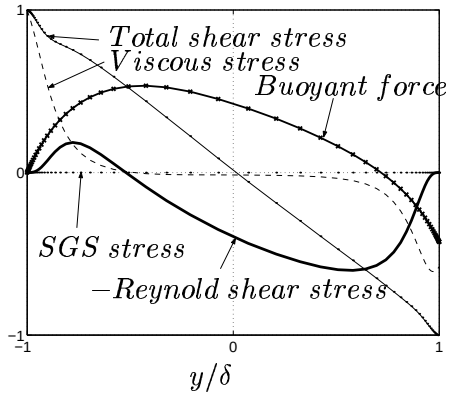


**Figure 5.29.** Stress balance in a wall-normal direction (vertical channel), $Re_\tau = 133$.

$$\underbrace{\left\langle \frac{\partial k}{\partial t} \right\rangle}_{=0} = - \underbrace{\langle uv \rangle \frac{\partial \langle \overline{u} \rangle}{\partial y}}_{Shear\ production} - \underbrace{\frac{\partial}{\partial y}\langle vk \rangle}_{Turbulent\ diffusion} + \underbrace{\nu \frac{\partial^2 \langle k \rangle}{\partial y^2}}_{Viscous\ diffusion} - \underbrace{\frac{1}{\rho}\frac{\partial}{\partial y}\langle vp \rangle}_{Presure\ diffusion} \underbrace{- \nu \left\langle \frac{\partial u_i}{\partial x_j}\frac{\partial u_i}{\partial x_j} \right\rangle}_{Dissipation} + \underbrace{\frac{Gr}{8 \cdot Re_\tau^{*2}}\langle vT \rangle}_{Buoyancy\ production} \tag{5.4}$$

where each term from equation 5.4 are shown in figure 5.30.[9] As noted in [5], the shear production term is clearly different from the opposite to the aiding side and it is twice as large on the opposing than on the aiding flow. All other terms shows the same behavior with decreasing in the aiding and increasing in the opposite flow. Note that the buoyant production is much smaller than the buoyancy term in the momentum equation, 5.2.

The budget equation of the temperature variance, $\langle T^2 \rangle$, given as:

[9]Note thet the dissipation term is computed as the balance term.

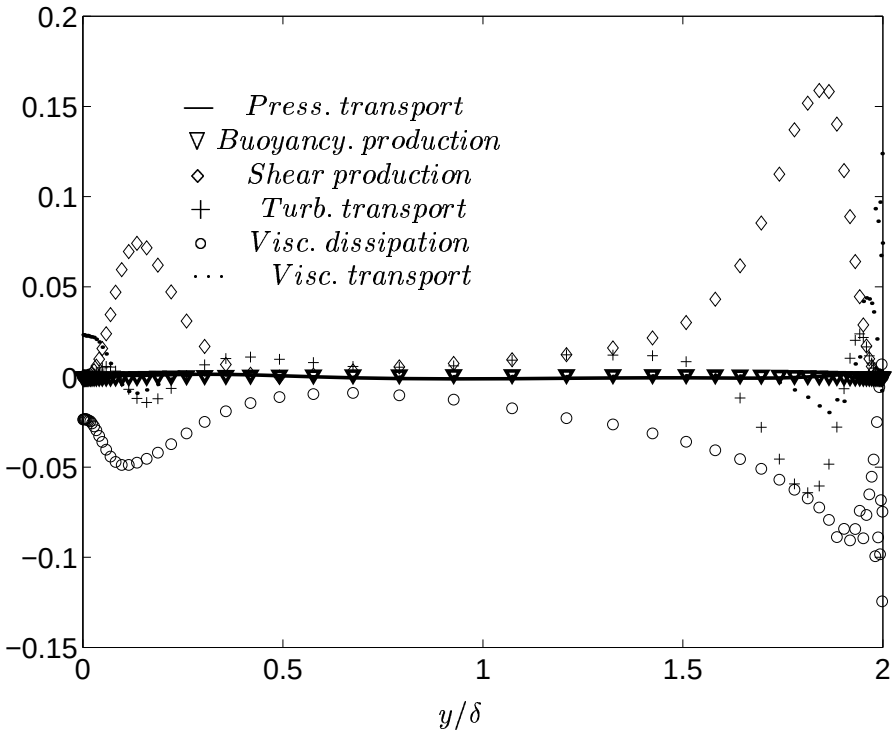


**Figure 5.30.** $\langle k \rangle$ balances, ($Re_\tau = 133$).

$$\underbrace{\frac{\partial \langle T^2 \rangle}{\partial t}}_{=0} = \underbrace{-\frac{\partial}{\partial y}\left[\langle vT^2 \rangle - 2\langle T \rangle \langle vT \rangle\right]}_{Turbulent\ diffusion} + \underbrace{\frac{1}{Re_\tau^* Pr}\frac{\partial^2}{\partial y^2}\left(\langle T^2 \rangle - \langle T \rangle^2\right)}_{Viscous\ diffusion}$$
$$\underbrace{-2\langle vT \rangle \frac{\partial}{\partial y}\langle T \rangle}_{Production\ by\ temperature\ gradient} + \underbrace{\frac{\nu_{SGS}}{Pr_t}\frac{\partial^2}{\partial y^2}\left(\langle T^2 \rangle - \langle T \rangle^2\right)}_{SGS\ viscous\ diffusion} \tag{5.5}$$
$$\underbrace{-\frac{1}{Re_\tau^* Pr}\left(\left\langle \frac{\partial T}{\partial y}\frac{\partial T}{\partial y}\right\rangle - \left\langle \frac{\partial T}{\partial y}\right\rangle \left\langle \frac{\partial T}{\partial y}\right\rangle\right)}_{Viscous\ dissipation}$$

Each term from equation 5.5 is shown in figure 5.31. There is no big difference between the opposing and the aiding side. Only production by the temperature gradients term is slightly different but it has the same peak value. All other terms have almost the same values on the opposite and the aiding side.

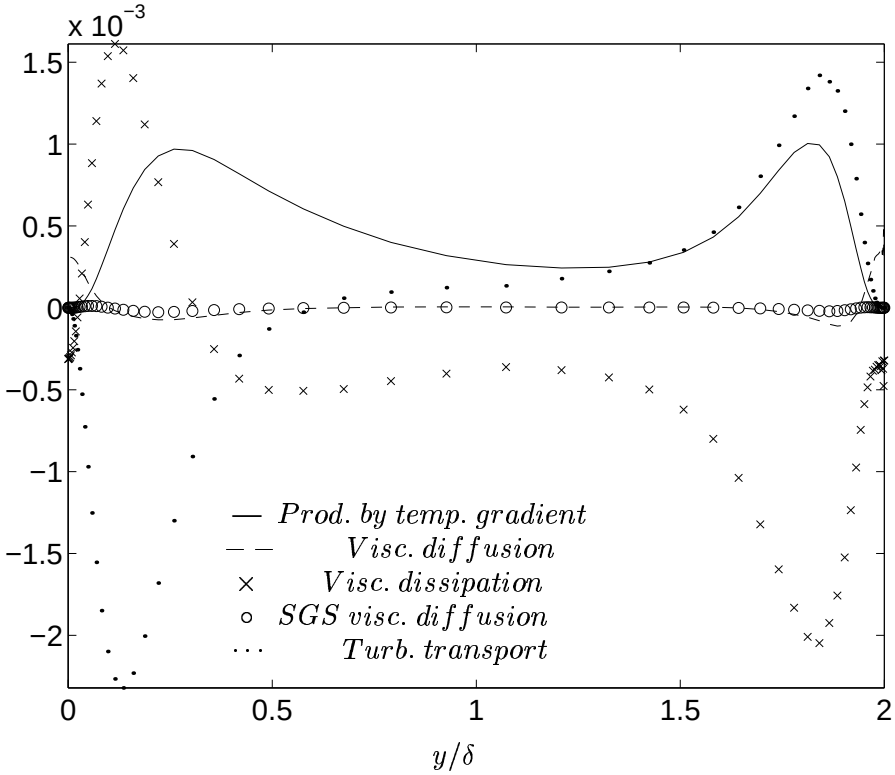


**Figure 5.31.** $\langle T^2 \rangle$ balances, ($Re_\tau = 133$).

# 6 Conclusions

The LES of the fully developed turbulent channel flow with scalar transport and combined force and natural turbulent convection was performed. The molecular Prandtl number is $0.71$ and Reynolds numbers are $Re_\tau = 395$ and $Re_\tau^* = 150$ . The following conclusions have been made:

- The LES gives a very good results in comparison with the DNS and can be used for simulation of the fully developed turbulent channel flow with uniform heating.
- The buoyancy force has significant effect on the mean flow causing remarkable changes in the near-wall region.
- The asymmetrical behavior of the Reynolds shear stress can be explained and understod in a better way by influence of the buoyancy force.
- The remarkable, opposite effect of decreasing buoyancy term on the mean flow was noted.
- The LES simulation can be used with much coarser grid size than the DNS.

# 7 Future Work

Next step should be that to increase/decrease the pressure gradient $\frac{\partial p}{\partial x} + C$ with the some constant values, $C$, until we obtain the required wall shear velocity, $u_\tau^* \ (= 1)$.

Some refinement of the mesh can be attempted to check if that can be reason why the LES and DNS do not agree.

One more calculation may be done with longer channel length to check if periodical conditions are the reason for some disagreements in comparison of the LES results with the DNS data.

The balances for more quantities should be calculated for better understanding of buoyancy influence on the channel flow.

The simple Smagorinsky model is tested in the present cases and another SGS method (dynamics) should be tested, see [8, 9]. Or maybe try to test the channel flow without SGS model at all since the subgrid-scales stresses only account for a small fraction of the total stresses when the grid is fine enough.

Then, two purposes should be done:

- To numerical explore (in detail) the buoyancy-driven or significantly affected turbulent flow and heat transfer features.
- To analyze the subgrid-scale motion in such flows and to model its behavior and effects on resolved large scales so as to improve and expand the capability of present LES methods to handle such flows.

# References

[1] H. Kawamura, H. Abe and Y. Matsuo. DNS of turbulent heat transfer in channel flow with respect to reynolds and prandtl number effect. *Int. J. of Heat and Fluid Flow*, 20:1996–207, 1999.

[2] J. Boussinesq. Théorie de l'Écoulement tourbillant. *Mem. Présentés par Divers Savants Acad. Sci. Inst.*, 23:46–50, 1877. France.

[3] L. Davidson. Hybrid LES-RANS: A combination of a one-equation SGS model and a $k-\omega$ model for predicting recirculating flows. In *ECCOMAS CFD Conference*, Swansea, U.K., 2001.

[4] P. Emwin and L. Davidson. Development and implementation of a fast large eddy simulations methods. rept. *Dept. of Thermo end Fluid Dynamics Chalmers University of Technology*, 1997.

[5] N. Kasagi and M. Nishimura. Direct numerical simulation of combined forced and natural turbulent convection in a vertical plane channel. *Int. J. of Heat and Fluid Flow*, 18:88–99, 1997.

[6] A. N. Kolmogrov. Local structure of turbulence in incompressible viscous fluid for very large reynolds number. *Doklady Akademiya Nauk, SSSR*, 30:299–303, 1941.

[7] S. Krajnović. Large-eddy simulation of the flow around a surface-mounted single cube in a channel. Diploma work Nr 98/7, Dept. of Thermo end Fluid Dynamics, Chalmers University of Technology, Gothenburg, Sweden, May 1998.

[8] D. Lilly. A proposed modification of the germano subgrid-scale closure method. *Physics of Fluids*, A 4:633–635, 1992.

[9] M. Germano, U. Piomelli, P. Moin and W. Cabot. A dynamic subgrid-scale eddy viscosity model. *Physics of Fluids*, A 3:1760–1765, 1991.

[10] S.V. Patankar. *Numerical Heat Transfer and Fluid Flow*. Hemisphere Publishing Corporation, Teylor & Francis Group, New York, 1980. ISBN 0-891-16522-3.

[11] U. Piomelli and J.R. Chasnov. Large-eddy simulation: Theory and applications. In Kluwer Academic Publishers, editor, *Turbulence and Transition Modelling*, pages 269–336. In ERCOFTAC serie, 2, 1995.

[12] M.J. Rhie and W.L. Chow. A numerical study of the turbulent flow past an isolated airfoil with trailing edge separatuon. *AIAA Journal*, 21:1525–1532, 1983.

[13] U. Schumann. Subgrid scale model for finite difference simulations of turbulent flows in plane channels and annuli. *J. Comp. Physics*, 18:376–404, 1975.

[14] J. Smagorinsky. General circulation experiments with the primitive equations: I. *Monthly Weather Review 91*, pages 99–165, 1963.

[15] A. Sohankar and L. Davidson. Effect of inclined vortex generators on heat transfer enhancement in a three-dimensional channel. *Numerical Heat Transfer. Part A*, 39(5):433 – 448, 2001.

[16] H.K. Versteeg and W. Malalasekera. *An introduction to Computational Fluid Dynamics*. Longman Group Ltd, England, 1995. ISBN 0-582-21884-5.

[17] I. Zacharov. Private communicaton. European Supercomputer Team, 1997.

# Appendix A:

The time history and the CFL number in the middle of channel for the horizontal flow ($i = 32, j = 32, z = 32$) and near-wall for the vertical channel ($i = 4, j = 18, z = 4$).

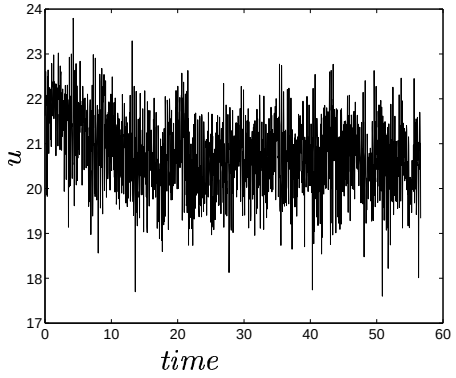


**Figure A.1.** Time history for $u$, $Re_\tau = 395$.

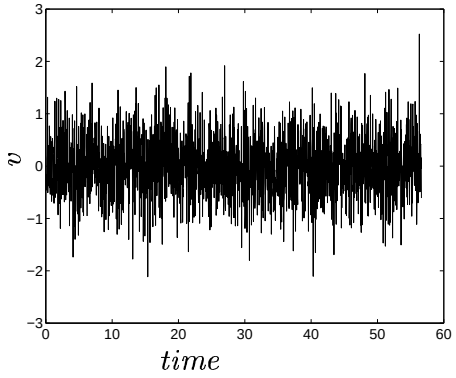


**Figure A.2.** Time history for $v$, $Re_\tau = 395$ .

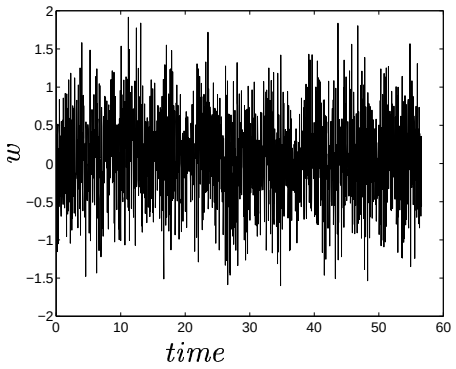


**Figure A.3.** Time history for $w$, $Re_\tau = 395$.

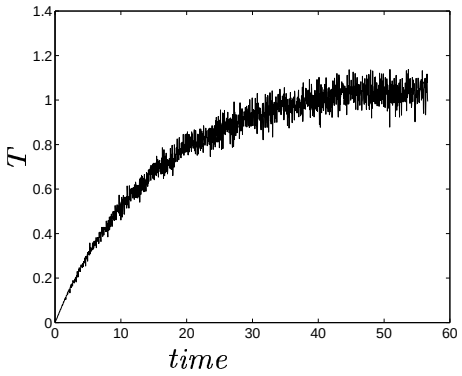


**Figure A.4.** Time history for $T$, $Re_\tau = 395$.

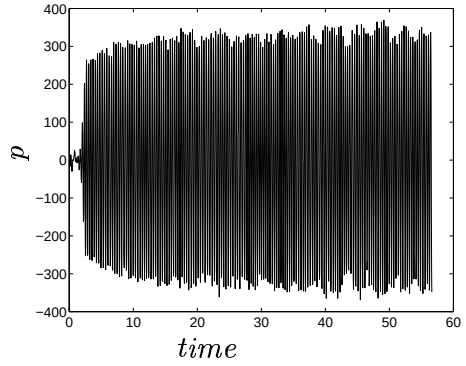


**Figure A.5.** Time history for $p$, $Re_\tau = 395$.

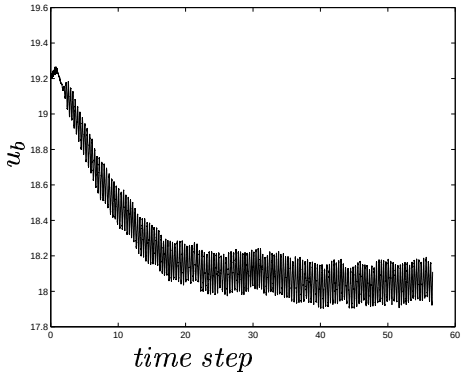


**Figure A.6.** Time history for $u_b$, $Re_\tau = 395$.

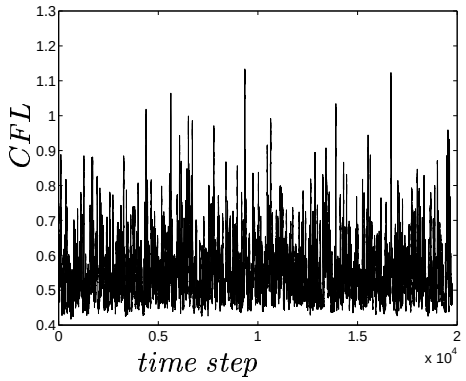


**Figure A.7.** Time history for $CFL$ number, $Re_\tau = 395$.

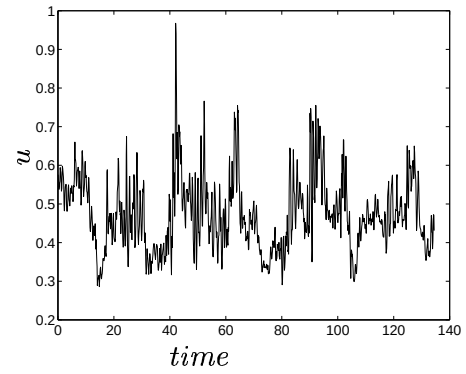


**Figure A.8.** Time history for $u$, $Re_\tau = 133$.

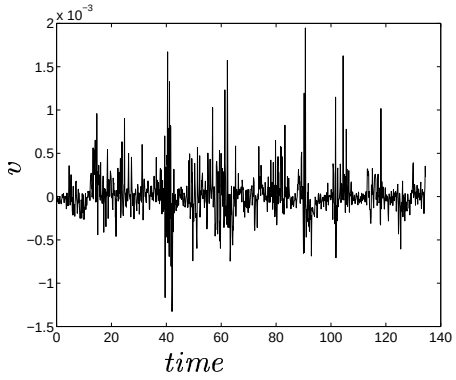


**Figure A.9.** Time history for $v$, $Re_\tau = 133$ .

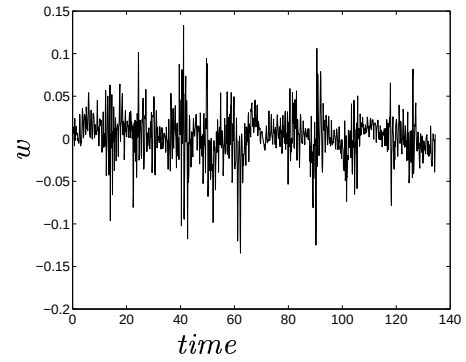


**Figure A.10.** Time history for $w$, $Re_\tau = 133$.

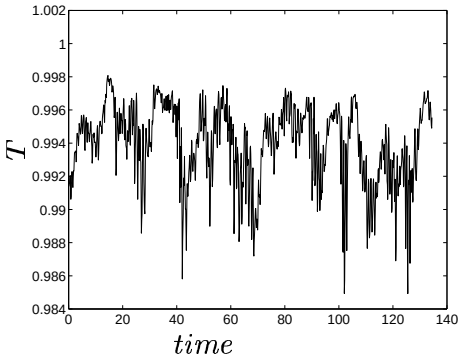


**Figure A.11.** Time history for $T$, $Re_\tau = 133$.

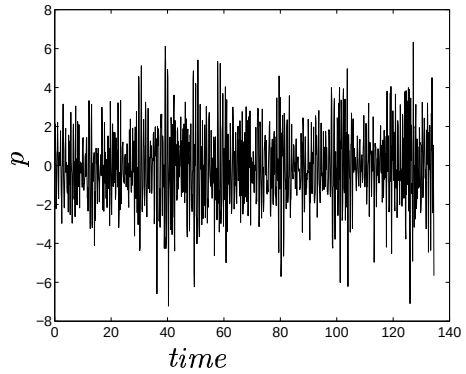


**Figure A.12.** Time history for $p$, $Re_\tau = 133$.

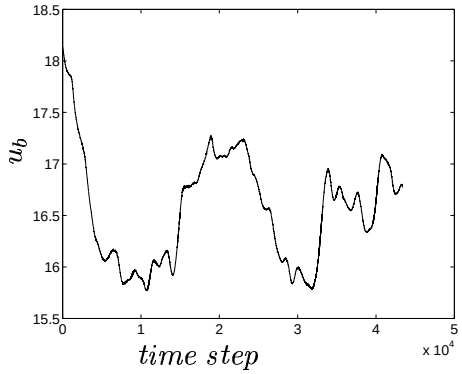


**Figure A.13.** Time history for $u_b$, $Re_\tau = 133$.

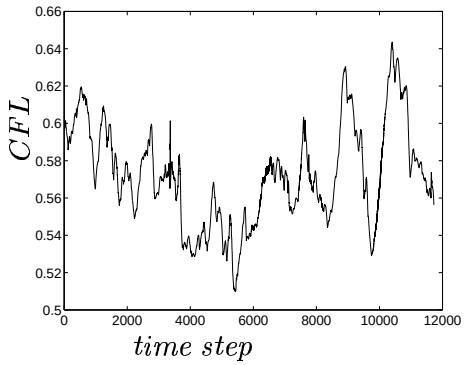


**Figure A.14.** Time history for $CFL$ number, $Re_\tau = 133$.

# Appendix B:

Comparison between the averaged values taken in a different time intervals (see figure A.13) where:

- dashed line (ts2) is in the interval between $8.000$–$16.500$ time steps,
- dot line (ts3) is in the interval between $16.500$–$24.000$ time steps and
- solid line (ts1) is in the interval between $20.000$–$43.000$ time steps.

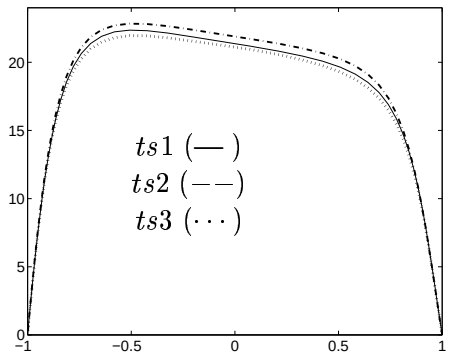


**Figure B.1.** Mean velocity profile in global coordinates in different time intervals, $Re_\tau = 133$.

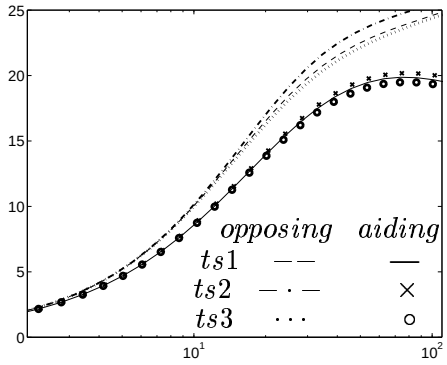


**Figure B.2.** Mean velocity profile in wall coordinates in different time interval, $Re_\tau = 133$.

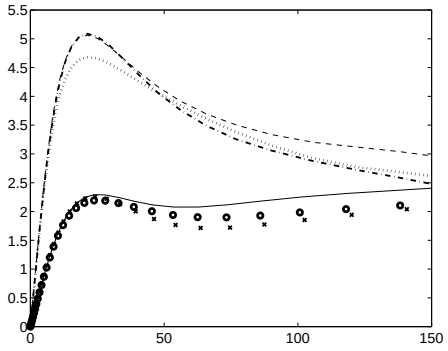

**Figure B.3.** $u_{rms}$ velocity profile in different time interval, $Re_\tau = 133$. For legend, see figure B.2

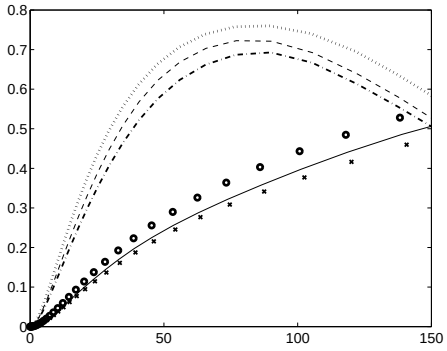

**Figure B.4.** $v_{rms}$ velocity profile in different time interval, $Re_\tau = 133$. For legend, see figure B.2

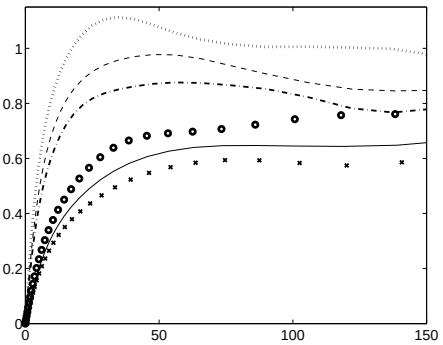


**Figure B.5.** $w_{rms}$ velocity profile in different time interval, $Re_\tau = 133$. For legend, see figure B.2

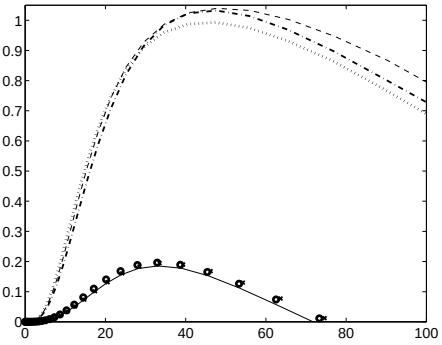


**Figure B.6.** Reynolds shear stress in different time interval, $Re_\tau = 133$. For legend, see figure B.2

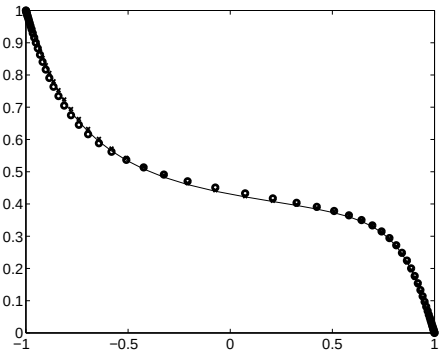


**Figure B.7.** Mean temperature profile in different time interval, $Re_\tau = 133$. For legend, see figure B.1

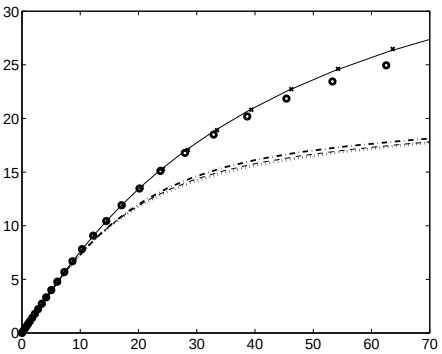


**Figure B.8.** Mean temperature profile in wall coordinates in different time interval, $Re_\tau = 133$.

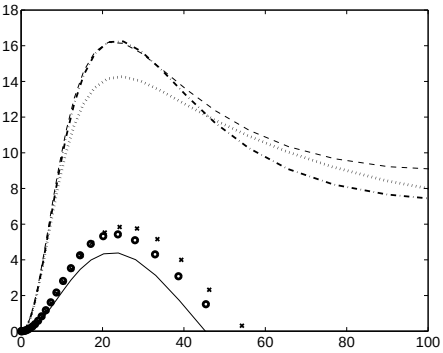


**Figure B.9.** Turbulent heat flux vector in a stream-wise direction in different time interval, $Re_\tau = 133$. For legend, see figure B.2

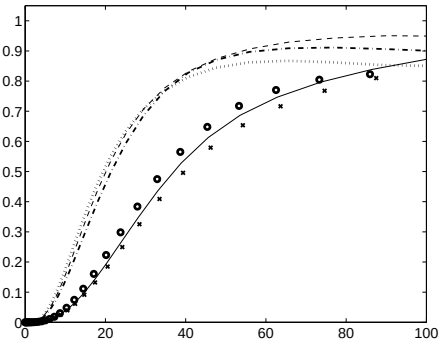


**Figure B.10.** Turbulent heat flux vector in a wall-normal direction in different time interval, $Re_\tau = 133$. For legend, see figure B.2

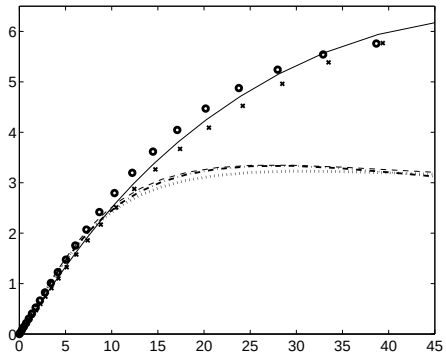


**Figure B.11.** Rms temperature profile in different time interval, $Re_\tau = 133$. For legend, see figure B.2

# Appendix C:

Averaged velocity fields and isothermal contours for the horizontal and the vertical channel.

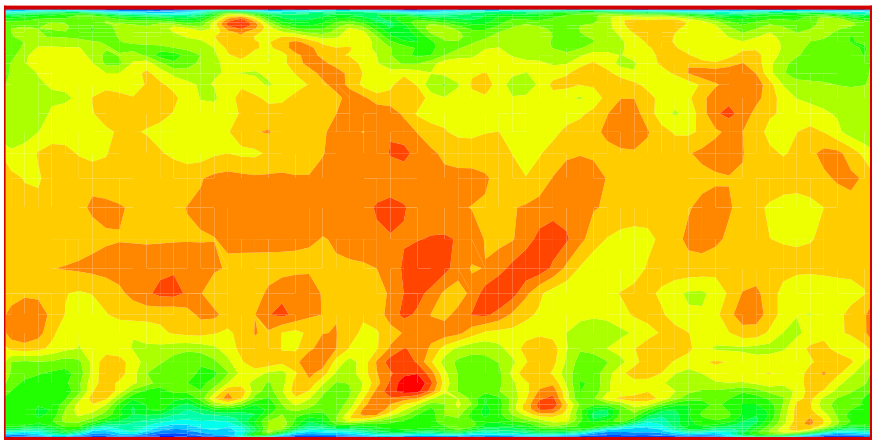

**Figure C.1.** Isothermal contour in the horizontal channel.

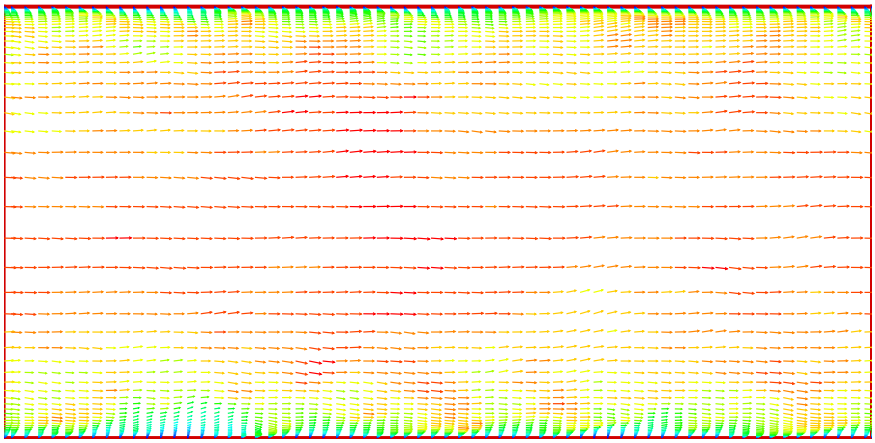

**Figure C.2.** Velocity field in the horizontal channel.

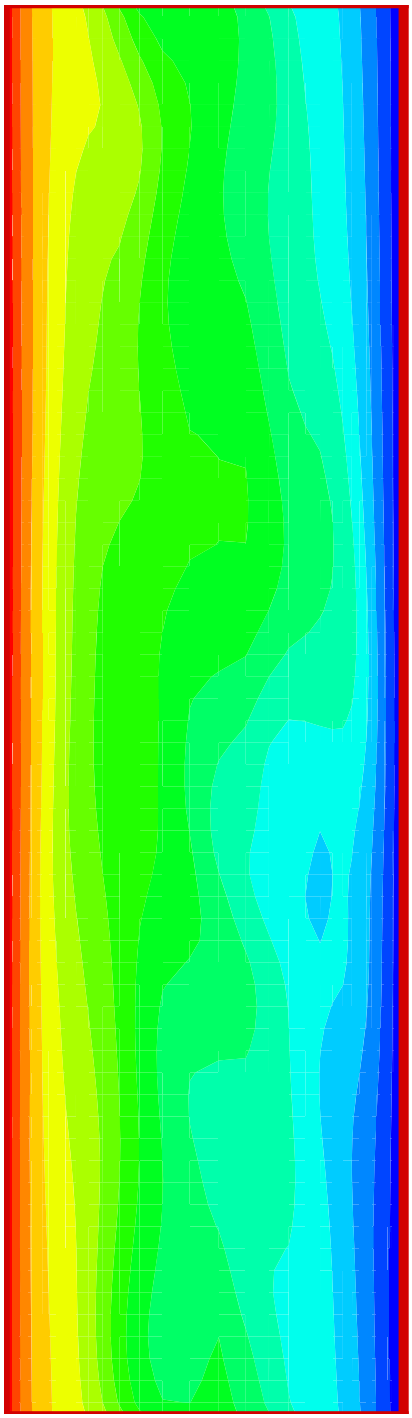

**Figure C.3.** Isothermal contour in the vertical channel.

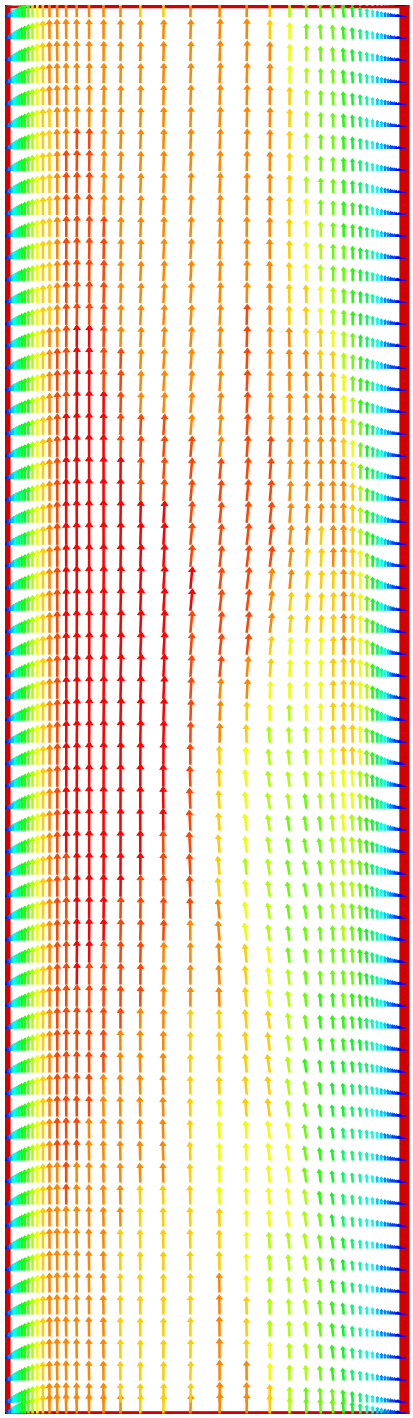

**Figure C.4.** Velocity field in the vertical channel.